Development of Multi-Frequency-Excitation Dynamic Nuclear Polarization (DNP)-NMR Methods: Improving DNP Efficiency and Spatial Selectivity

周波数複合励起・動的核偏極(DNP)-NMR 法の開発：DNP 効率と空間選択性の向上

Graduate School of Science

Osaka University

2023

Zhongliang Zhang

Table of Contents

0. Abstract

This dissertation focuses on utilizing multi-frequency-excitation microwave (MW) to enhance Dynamic Nuclear Polarization (DNP) efficiency and spatial selectivity. The unique advantage of NMR spectroscopy is its capacity to elucidate the structure and function of target molecules within complex mixtures, without the need for isolation or purification processes. However, this application of NMR spectroscopy is not without challenges, particularly concerning signal overlap and sensitivity issues. To mitigate these challenges, DNP, a technique commonly employed to amplify NMR signals, can be utilized. Despite its ability, DNP only partially addresses these issues. Considering the availability of advanced frequency-agile MW sources in our laboratory, the utilization multi-frequency-excitation MW presents a viable direction for the exploration.

Although DNP can selectively enhance the NMR signals of target molecules by specifically binding the polarizing agent to them, the presence of background molecules in mixed samples can still produce substantial background signals, potentially interfering with the analysis of target signals. To address this, a novel method for background signal suppression is introduced to enhance the selectivity of DNP- NMR spectroscopy in the investigation of target molecules within complex mixtures. This approach uses the subtraction of positively and negatively enhanced DNP spectra, resulting in a significant improvement in the contrast factor, defined as the ratio between the intensities of the target and background signals. The efficacy of this method was experimentally validated using a reverse-micelle system that encapsulates the target molecules alongside the polarizing agent, OX063 trityl. A great increase in the contrast factor was observed with careful selection of the DNP

build-up time. A subsequent simulation study, based on the experimental outcomes, offers valuable insights into the methodology for selecting the optimal DNP build-up time and the method's corresponding selectivity. Further exploration of this technique revealed its wide-ranging applicability, extending to the study of large biomolecules and surface-modified polymers, with its effectiveness varying according to the nuclear spin diffusion rate across different gyromagnetic ratios. This broad applicability underscores the potential of this method to advance the field of DNP-NMR spectroscopy to study targets in complex mixtures.

To detect target molecules within mixtures, the sensitivity of the target can still be an issue even under DNP enhancement, as the quantity of target molecules can be too low among the large number of molecules in the mixture. This necessitates a further improvement in the DNP efficiency. I employed spin dynamic simulations to explore the potential application of multi-frequency excitation MW to amplify DNP enhancement. The study simulates DNP enhancement frequency profiles across a variety of scenarios. This includes a demonstration of the ineffectiveness of using frequency sweep MW to augment solid effect DNP enhancement under Magic Angle Spinning (MAS), and a further investigation of the underlying reasons for the ineffectiveness. And subsequent simulations revealed that in more complex scenarios involving polarizing agents, the use of multi-frequency-excitation MW can indeed enhance DNP efficiency. For instance, scenario where the mixture contains two types of polarizing agents with different g tensors, multi-frequency-excitation MW, serving as a complement to MAS, can improve the enhancement of solid effect DNP. And another example, when employing Mn(II) as the polarizing agent, the solid effect DNP matching conditions, which are split due to isotropic hyperfine interaction, do not shift with MAS. Consequently, the irradiation of these multiple matching

conditions with multi-frequency-excitation MW can greatly increase DNP enhancement, providing the MW power is high enough.

Overall, the research demonstrated the potential of multi-frequency-excitation DNP for both higher DNP efficiency and spatial selectivity.

1. General Introduction

1.1 Overview of NMR Spectroscopy in Complex Mixtures

Nuclear Magnetic Resonance (NMR) Spectroscopy, grounded in quantum mechanics and the magnetic properties of atomic nuclei, is a powerful analytical tool. [1–3] Central to NMR is the concept of spins, which, in the presence of a magnetic field, aligns in specific energy states. Radiofrequency (RF) pulses cause nuclei with a magnetic moment to absorb energy, transitioning between these states, forming coherence that is vital to the extraction of information and detection of NMR signal, the free induction decay (FID). The FID detected is Fourier transformed into an NMR spectrum. The sensitivity of this process to the surrounding chemical environment makes NMR an invaluable tool for understanding molecular structure in atomic resolution.

The NMR signal intensity originates from the initial difference of spin population in energy states, which are divided by magnetic field. It can be described by polarization. For spin I = 1/2, polarization can be defined as the difference of α and β state population over the total population $P = \left(N_\alpha - N_\beta\right)/\left(N_\alpha + N_\beta\right)$. Under thermal equilibrium, the spin population follows Boltzmann distribution so that $N_\alpha \propto \exp(\hbar\gamma B_0/2kT)$ and $N_\beta \propto \exp(-\hbar\gamma B_0/2kT)$. Then, polarization $P = \tanh(\hbar\gamma B_0/2kT)$, where $\hbar$ is the reduced Planck constant, γ is the spin's gyromagnetic ratio, B_0 is magnetic field strength, k is the Boltzmann constant and T is temperature. Thus, under certain magnetic field and temperature, high γ spin has higher polarization than low γ spin. Specifically, under high temperature approximation, polarization is proportional to the gyromagnetic ratio γ. The polarization under thermal equilibrium is then related to NMR signal intensity.

NMR spectroscopy's applications extend beyond structural analysis, offering insights into molecular dynamics, interactions, and reaction mechanisms. By analyzing longitudinal relaxation time, the period nuclear spins return to equilibrium after an RF pulse, and transverse relaxation time, the period nuclear spins loss their coherence, researchers glean information about molecular motion and interactions. This technique is indispensable in fields ranging from chemistry and biology to materials science and medicine, favored for its non-destructive nature and minimal sample preparation. For example, NMR spectroscopy is widely used in structural biology, which focuses on the study of structure and function of bio-micromoles, such as proteins.

There are two primary forms of NMR spectroscopy: solution NMR and solid-state NMR. The choice between these forms depends on the sample and desired information. Solution NMR is effective for analyzing molecules up to small and soluble proteins, offering high-resolution spectra due to the free Brownian tumbling of molecules in solution. This movement averages out many spin interactions, leading to narrower spectral lines and clearer structural insights for small molecules. On the other hand, solid-state NMR doesn't require samples to be soluble and is excellent for studying larger or more complex structures like membrane proteins, or amyloid fibrils. Furthermore, solid-state NMR can provide detailed information about the physical properties of solids, which are critical in materials science and polymer chemistry. [4,5]

In solid-state samples, the limited molecular motion results in broader spectral lines due to unaveraged spin interactions. This broadening can be mitigated using magic-angle spinning (MAS),[6] enhancing resolution of NMR spectroscopy. For MAS of moderate spinning rate (~20 kHz), ^{1}H detection in solid-state NMR often doesn't yield

sufficient resolution and detection of low γ nuclear spin such as ^{13}C spin is more feasible. Technique called cross-polarization[7] transferring polarization from high γ nuclear spin to low γ nuclear spin can be used to compensate the relatively low sensitivity of low γ nuclear spin detection.

The function of bio-macromolecules depends on their 3D structure and dynamic with time scale ranges from picoseconds to seconds. NMR spectroscopy can access the entire time scale by investigating various kinds of NMR phenomena and interaction. Thus, NMR spectroscopy is a key method for elucidating structure and dynamic of bio-macromolecules.[8,9] Other techniques providing atomic level resolution, such as X-ray crystallography are ideal for obtaining high-resolution structures when crystals are available, and cryo-EM has advanced to analyze mono-dispersed high-molecular-weight biomolecule complexes.[10] Compared to these techniques, NMR spectroscopy's uniqueness lies in its ability to characterize molecular structures at atomic resolution within mixtures, without needing isolation or purification.[11,12] This feature is crucial for the NMR measurements of biomacromolecules *in situ*,[13,14] referred as in-cell NMR. In-cell NMR is an important topic in structural biology, enabling the study of proteins in their natural cellular environment, providing insights into how such environments influence protein structure and behavior. This approach acknowledges that protein structures and dynamics within a crowded intracellular might differ from those in purified solutions,[15–17] which have historically been used for the analysis of proteins. Also, the polymorph of protein aggregates or fibrils is strongly affected not only by the primary sequence but also by the intracellular environment.[18,19]

Despite its strengths, NMR faces significant challenges when studying small amounts of target molecules in complex mixtures. Signal overlap, where signals from different

molecules interfere with each other, and sensitivity, the ability to detect signals from low-abundance species, are the primary challenges, because the target molecules are naturally diluted by a large number of background molecules. An example of the difficulty of the in-cell NMR is that it wasn't until 2009 that a landmark study[15] first elucidated the structure of a model protein within *Escherichia coli* using solution-state NMR. For in-cell solid-state NMR (Figure 1.1.1), no structure determination has been reported yet. As the solid-state NMR further exacerbates the problems of signal overlap and low sensitivity due to the difficulty in ^{1}H signal detection and the generally smaller active sample volume in an MAS rotor.

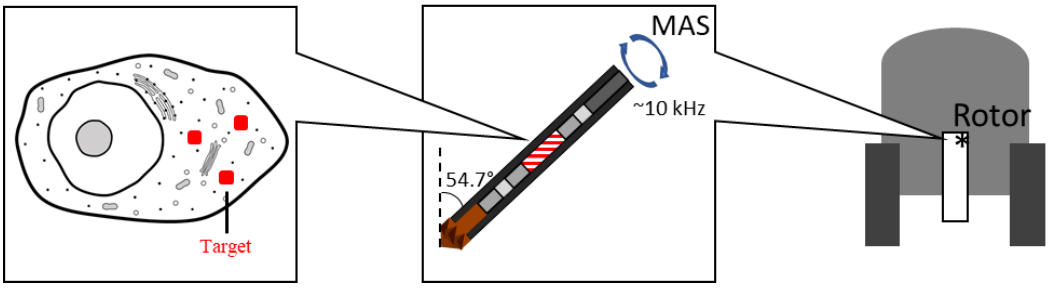

Figure 1.1.1 Schematic for *in-cell* solid-state NMR.

In in-cell NMR studies, the issue of low sensitivity and low selectivity is severe (Figure 1.1.2). For example, the most expressed protein TDH3 in budding yeast (*Saccharomyces cerevisiae*) has 1.6 million copies per cell.[20] Suppose a 3.2 mm MAS rotor can contain 20 μL sample and a volume of a yeast cell is 86 μm^3.[21] Then there are about 3.7×10^{14} copies in the sample, which is only 3.7% of the solid-state NMR detection limit, supposing the detection limit is 10^{16} spins. If natural abundance ^{13}C is considered, then the detection limit will raise to 10^{18} spins. Complex NMR

experiments will further raise the detection limit. The molecular mass of TDH3 is 35.7 kDa, and the dry mass of a single budding yeast is about 50 pg.[22] Thus, the mass of TDH3 is only 0.19% of the dry mass of budding yeast cell. The background signal from other components in cells is expected to be greatly larger than a specific type of protein. These issue can be somewhat mitigated by overexpressing the target protein within the cells or introducing purified target protein into the cells.[23] They are also the necessary procedures for the selective isotopic labeling of the target protein.[24,25] However, the overexpression limit of, for example, the aforementioned TDH3 is estimated to be 4.3 times,[20] which is still much lower than the detection limit. And overexpressing excessively high concentration of the protein or introducing exogenous protein in the cytoplasm deviate from the original intent of studying the protein in its natural state, as the concentration of the target protein is sometimes crucial to its structure and dynamics.[18,26,27]

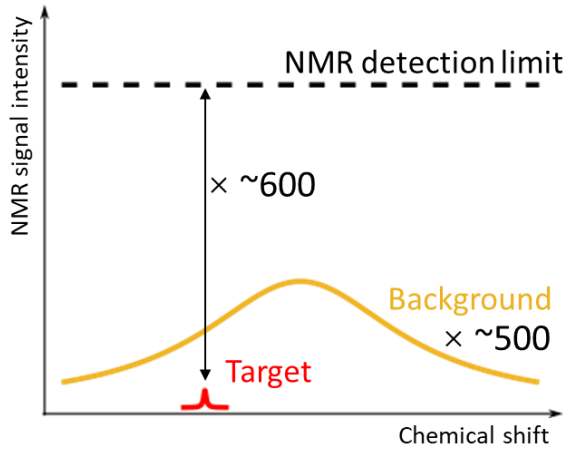

Figure 1.1.2 Schematic shows low sensitivity and low selectivity issues of natural abundance ^{13}C *in-cell* solid-state NMR.

In summary, exploring new technological approaches to address the challenges of signal overlap and sensitivity in NMR studies of mixtures is crucial for leveraging the

full potential of NMR spectroscopy.

1.2 DNP Mechanism in Solid-State NMR

The dynamic nuclear polarization (DNP) technique has significantly advanced over the past decades to enhance the sensitivity of NMR by approximately two orders of magnitude. Like the idea of cross-polarization that transfer polarization from high γ nuclear spin to low γ nuclear spin, the idea of DNP is to utilize the electron spin, which has much higher γ value than that of nuclear spin. It is achieved through the application of microwaves (MWs) of proper frequency, that transfers the high electron-spin polarization of polarizing agents (PAs) to adjacent nuclear spins. Following this initial transfer, spin diffusion propagates the polarization further to nearby nuclear spins, leading to a substantial enhancement in NMR signals within the range of spin diffusion (Figure 1.2.1).[28–30]

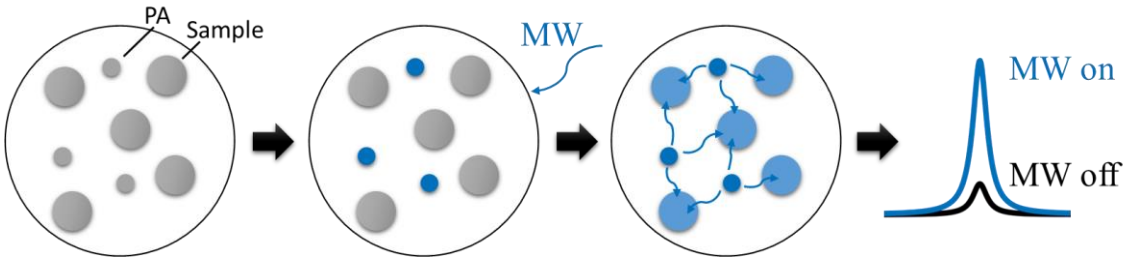

Figure 1.2.1 Schematic of DNP process.

The DNP enhancement, defined as the ratio of NMR signal with to without MW irradiation, can theoretically be as high as the ratio of thermal equilibrium state electron spin polarization to nuclear spin polarization $\tanh(\hbar\gamma_e B_0/2kT)/$

$\tanh(\hbar\gamma_n B_0/2kT)$, which is approximately γ_e/γ_n under high temperature. Practically, the DNP enhancement is subject to various conditions and thus, be much lower than this upper limit.

At the core of the DNP mechanism is the use of PA, a molecule characterized by its unpaired electrons. These agents can vary in form, ranging from radicals, either monoradical or biradical[31] to paramagnetic metal complexes,[32,33] or even nanodiamonds,[34,35] where defects or dangling bonds on the surface of nanodiamond contribute unpaired electrons. The DNP-NMR experiments begin with the mixing of the polarizing agent with the sample under examination. These unpaired electrons of the PA exhibit direct hyperfine coupling with nearby nuclear spins, which are, in turn, connected to further nuclear spins through networks of dipolar coupling. When the mixture is irradiated by MW at a frequency resonant with electron spin, the significantly higher polarization of the electron spins, attributable to a much greater gyromagnetic ratio, is transferred to adjacent nuclear spins.

This transfer as the commencement of the DNP process has been extensively researched. In solid-state NMR, the mechanisms of the DNP transfer mainly include Solid Effect (SE),[36] Cross Effect (CE),[37,38] and Thermal Mixing (TM).[39] The energy level diagram for SE and CE are shown in Figure 1.2.2. The SE occurs in a two-spin system, consisting of one electron spin and one nuclear spin. When MW irradiation is applied at a frequency equal to the sum of the electron and nuclear spin resonance frequencies, a forbidden Zero-Quantum (ZQ) transition is induced. This transition transfers population from the beta-alpha state to the alpha-beta state, leading to a saturation of the population difference between these states. This causes the population difference between alpha-beta state and alpha-alpha state (also the

population difference between beta-beta state and beta-alpha state) to be negative and its absolute value much larger than that of the thermal equilibrium condition. This process results in a negative enhancement. Conversely, applying MW at a frequency equal to the difference between the electron and nuclear spin resonance frequencies induces a forbidden Double-Quantum (DQ) transition. This results in a higher population of the nuclear alpha state compared to the beta state, leading to positive enhancement. The SE is the main DNP mechanism that is employed and discussed in this dissertation.

The CE occurs in a three-spin system, involving two electron spins and one nuclear spin. MW irradiation at specific frequencies can saturate the population of one of the electron spins. If two of the three spins are at the same energy level, a three-spin flip-flop-flip (i.e. $|\alpha\beta\alpha\rangle \leftrightarrow |\beta\alpha\beta\rangle$) process occurs, transferring population between them and changing the population of nuclear spin states. Depending on the frequency of the MW irradiation, this can lead to either a negative enhancement (with higher population of nuclear beta state) or a positive enhancement (with higher population of nuclear alpha state).

TM is another mechanism in DNP. This mechanism becomes active when the electron resonance is broader than the nuclear Larmor frequency. It involves the transfer of polarization from multiple electron spins to nuclear spins. The TM process relies on a complex interplay of spin temperatures and energy flows between spins and the lattice. Due to the multiply electron and nuclear spins involved in the process, it is beyond the capability of simulation that will be discussed in this dissertation.

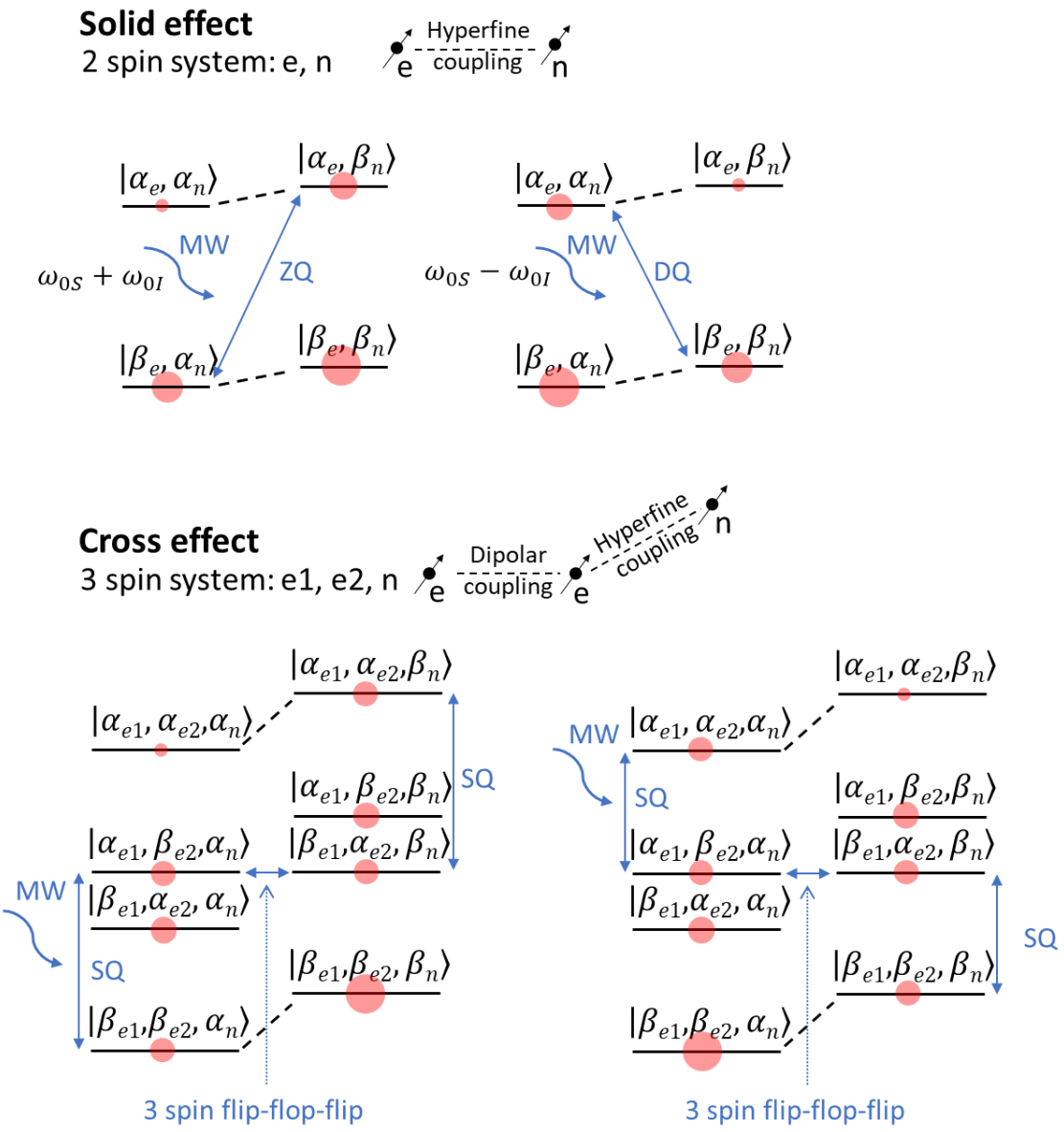

Figure 1.2.2 DNP mechanisms of SE and CE. The red circles represent the spin population of certain energy states. The difference of the spin population on energy states connected by dashed lines results in positive or negative DNP enhancement.

The anisotropy of interactions means that spin systems with different orientations relative to the external magnetic field have distinct energy levels. In a static sample, a spin system must satisfy the conditions of SE or CE to achieve enhancement. However, in a sample undergoing MAS, the energy levels fluctuate during the rotor

period, allowing spin systems to achieve enhancement if they meet the SE or CE conditions at any point during the rotation. This sensitivity to MW frequency and orientation diversity contributes to the characteristic DNP enhancement frequency profile.

The hyperpolarization caused by DNP is propagated by spin diffusion process.[40,41] Microscopically, the flip-flop interaction between two adjacent nuclear spins is governed by quantum dynamics. However, when viewed macroscopically, especially considering the vast number of nuclear spins involved, spin diffusion resembles a classical diffusion process. This analogy is the basis for the term "spin diffusion." This process can be described using classical diffusion equations, within which, a parameter diffusion rate D is used to describe how fast the diffusion is. When the nuclear spins experience direct DNP enhancement or the enhanced polarization from the propagation of spin diffusion are subjected to NMR detection, the sensitivity of NMR signal is enhanced.

1.3 Challenges in Solid-State DNP-NMR Efficiency and Selectivity

DNP significantly enhances NMR signal intensity, addressing sensitivity issue in NMR studies of target molecules complex mixtures. However, in these mixtures, the efficiency of DNP can be lower than expected. For instance, in in-cell DNP-NMR scenarios, radicals, which act as PAs, are easily reduced in the cytoplasm, leading to a rapid decline in DNP efficiency. One solution is to use PAs that are not prone to chemical reduction, such as paramagnetic metal complexes or nanodiamonds.[42] Nonetheless, the DNP efficiency of these stable PAs is usually not as high as the

generally used nitroxide based radicals. And DNP equipment using conventional fixed frequency gyrotron tuned for nitroxide based radicals is difficult to repurpose to the use of the paramagnetic metal complexes or nanodiamonds as PAs.

To enhance DNP-NMR efficiency, researchers are exploring several approaches, such as developing more efficient PAs and advanced DNP experimental methods. One approach, unlike conventional DNP that employs continuous wave (CW) MW on a single frequency, irradiating multiple frequencies using frequency-modulated MW has shown to give a better DNP enhancement.[43–46] For example, DNP methods referred to as integrated solid effect and stretched solid effect utilizes a SE under static conditions with SA-BDPA as the polarization PA. And a MW with a frequency sweep of 50 MHz results in a higher DNP enhancement compared to conventional approaches.[44] Another research implemented CE DNP under 10 kHz MAS and employed tethered TEMPO-trityl radical as the PA. The use of a 100 MHz frequency-swept MW generated by an Arbitrary Waveform Generator (AWG) leads leading to an increase in maximum DNP enhancement of up to 150% after powder averaging.[46] These techniques enable a more effective polarization transfer and potentially addressing the inefficiencies encountered in complex mixtures or in-cell environments. Though, the detailed application of multi-frequency excitation DNP methods in in-cell DNP-NMR scenarios remain an area that requires further exploration.

DNP also partially addresses the signal overlap issue in NMR studies for target molecules in complex mixtures. Targeted DNP is a method for solid-state NMR in biomolecular research where the PA is delivered site-specifically to the target molecules,[47–50] usually by specific binding or affinity of the PA to target. This selective delivery enables the preferential enhancement of signals from the target

molecules, distinguishing them more clearly from the surrounding background. In such a targeted DNP-NMR study in a mixture sample, a primary challenge is suppressing the relaxation-induced background signals from regions outside the diffusion range, which can interfere with or, depending on the size of the background, overwhelm the target signals. Although selective isotopic labeling of the target molecules and/or deuteration of the background can be employed, this approach is often difficult, expensive, and/or labor-intensive for in operando material samples or *in situ* cellular samples and is not always applicable. One possible solution is preparing another sample with ubiquitous distributed PA to measure the background signal and subtract it from the previous one. However, preparing two samples with different spin labels or PA distributions for data subtraction is not generally straightforward in practice for complex samples. Alternatively, data acquired without DNP (MW-off data) can be subtracted from the DNP-enhanced data (MW-on data) to remove the background. However, this method is inefficient because the MW-off data requires the same averaging time as the MW-on data to preserve the signal-to-noise (S/N) ratio after the subtraction; in addition, the subtraction will partially remove the target signals. Thus, an alternative method is needed to fully exploit the potential of DNP-NMR for targeted measurements in a mixture sample. In this dissertation, I will discuss an alternative approach I proposed that utilizes multi-frequency excitation MW in DNP to suppress background signals.

1.4 Introduction of DNP Using Multi-Frequency Microwave

As described above, multi-frequency MW irradiation in DNP shows promise in enhancing DNP efficiency and spatial selectivity, compared to conventional CW-MW

DNP. There are several well-researched types of multi-frequency MW. One example is chirped MW, a frequency-modulated MW that linearly sweeps across a frequency range during irradiation. Another is pulsed MW that alternates between or simultaneously irradiates two or multiple frequencies. These methods have been reported to improve DNP enhancement and are less affected by the decrease in DNP efficiency at higher magnetic fields. However, implementing such MW techniques introduces greater technical complexity, requiring specific MW sources for multi-frequency MW irradiation. These sources demand more sophisticated control, and optimizing their MW conditions often involves extensive experimentation. Additionally, their flexibility in manipulating electron spin dynamics usually results in lower MW power output compared to traditional CW-MW sources like gyrotrons.

A suitable MW source, for instance, might be a double-gyrotron setup (Figure 1.4.1(a)).[51] In 2016, our lab developed and reported on a 460 GHz-700 MHz DNP NMR spectrometer utilizing two gyrotrons, a frequency modulation gyrotron and a tunable gyrotron. This unique setup enables simultaneous or sequential irradiation with two different MW, merged into a single beam before entering the NMR probe. The double-gyrotron setup allows rapid frequency modulation over a range of a GHz, which surpasses the capabilities of a single tunable gyrotron. This dual-frequency irradiation is well-suited for various applications in multi-frequency MW DNP.

A solid-state MW source centered on Arbitrary Waveform Generator (AWG) and Amplifier Multiplier Chain (AMC) allows more versatile application (Figure 1.4.1(b)). Arbitrary Waveform Generator (AWG) is a sophisticated piece of electronic equipment.[46,52,53] Unlike standard function generators that produce predefined waveforms like sine or square waves, an AWG can generate almost any waveform,

based on specific digital data stored in its memory and converted into waveforms in real-time by a digital-to-analog converter. This capability enables the creation of complex MW waveforms with varying amplitudes, frequencies, and even phases. The AWG is connected to the Amplifier Multiplier Chain (AMC) to produce MW of a few hundreds of GHz to be applicable in DNP under high magnetic field. The AWG also has a broader frequency range, often spanning several GHz. Its flexibility can be combined with optimal control techniques, which utilize sophisticated waveforms optimized from simulations or experiments to maximize DNP transfer efficiency. Considering that AWGs usually have much lower MW power compared to gyrotrons, it's possible to pair an AWG with a gyrotron for a frequency-agile system.[54] In this setup, the AWG can ramp the output frequency of the gyrotron, creating a chirped MW.

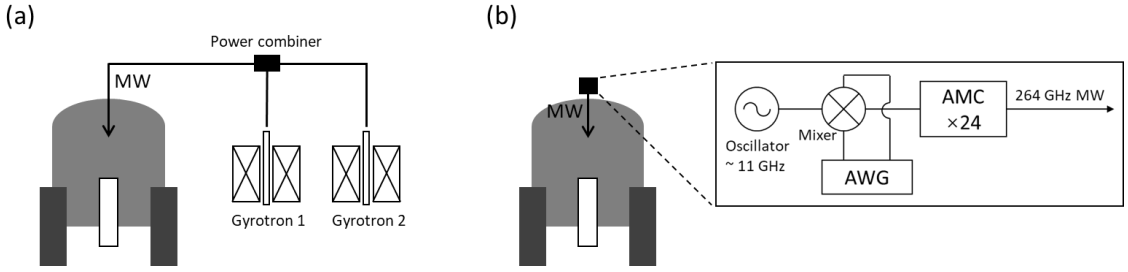

Figure 1.4.1 Schematic of the multi-frequency MW sources: (a) double gyrotron NMR system and (b) solid-state MW source.

1.5 Scope of the Dissertation

In this dissertation, I will focus on the DNP-NMR technique of utilizing multi-frequency MW to improve DNP efficiency and DNP spatial selectivity. The research

is based on the custom-built frequency-tunable gyrotron and anticipated multi-frequency MW source in our lab. Considering the potential future utilization of DNP-NMR for target molecules in cell or other complex environments, on Chapter 2, I will introduce a novel background signal suppression method to address the low selectivity issue and its validation by experiments and simulation, and on Chapter 3, I will present the simulation results that shows promise in improving DNP enhancement with multi-frequency MW to address the low sensitivity issue. More simulated results are expected to be put into validation with the development of the MW sources in the future.

2. Improving Spatial Selectivity

2.1 Principle of the Oops Method

I proposed an improved multi-frequency-excitation DNP approach to suppress not-of-interest background signals by taking the difference between the spectra of positively and negatively enhanced DNP (referred as positive and negative DNP) data. With many DNP mechanisms, including the solid effect (SE) and the cross effect (CE), the DNP can be selectively excited in opposite polarities by simply choosing an appropriate excitation MW frequency. This selective excitation is most practically achieved using the frequency tunability of the MW source, a gyrotron. I refer to this approach as "opposite polarity subtraction" (Oops), and it enables the selection of NMR signals from a "target region" responding to the polarity switch of the DNP while suppressing NMR signals from the "background region" outside the diffusion range, which arise purely from the spin relaxation. Compared with the MW-off data subtraction, the Oops treatment doubles the S/N ratio for the target signals in the same total experimental time. In addition, this approach enables the application of both positive and negative DNP on a single sample, thereby avoiding the challenges associated with preparing multiple samples.

Figure 2.1.1 schematically depicts the spatial distribution of the polarization around a PA molecule at a certain polarization build-up time. The electron spin at the origin produces positive (blue) or negative (red) DNP enhancement, and spin diffusion propagates this enhancement to the nearby nuclear spins. Outside the diffusion range, nuclear spins always relax toward a small positive value (i.e., the thermal equilibrium state) irrespective of the polarity of the hyperpolarization in the diffusion range (Figure 2.1.1a and b). Therefore, when the difference between the two (i.e., DNP(+) −

DNP(−) (the Oops procedure)) is taken, polarization accumulates in the target space while being canceled in the background space (Figure 2.1.1c and d). With this method, I can selectively enhance the NMR signals for the target molecules and suppress the NMR signals for the molecules in the background. Subtracting the MW-off data gives similar background signal suppression but only one-half of the target signal intensity (Figure 2.1.1d, green).

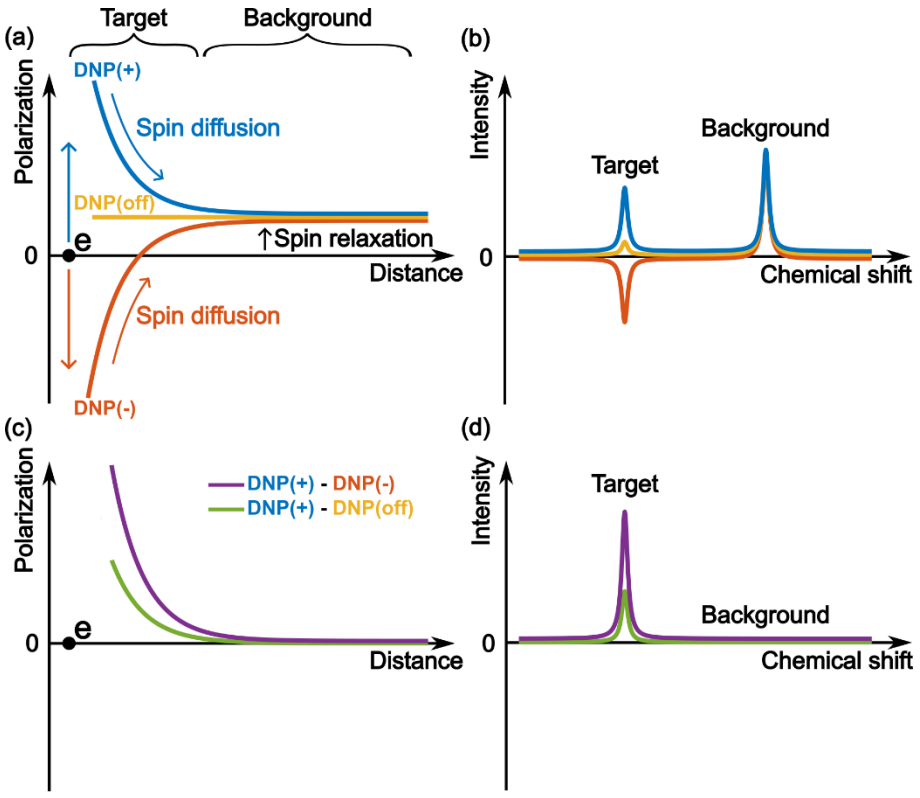

Figure 2.1.1 The mechanism of the background signal suppression by Oops. (a) Schematic of the spatial distribution of nuclear spin polarization centered around an unpaired electron spin, following either positive (blue) or negative (red) DNP, or without DNP (yellow). The space influenced by DNP, labeled as "Target," and the space unaffected, labeled as "Background," are indicated in the figure. (b) Schematic NMR spectra for positive and negative DNP and without DNP, corresponding to the spatial distribution shown in panel (a). (c) Result of the difference between the polarizations of positive and negative DNP (purple) and that between the polarizations of positive and MW-off (green). (d) The corresponding spectra.

2.2 Sample Preparation: Reverse Micelles and Nanodiamonds

To validate the Oops method, I used a reverse-micelle system that enables the target region to be defined relative to the background space in the sample. It emulates the case where the PA is delivered near the target molecule. I employed the water/sodium bis(2-ethylhexyl) sulfosuccinate (Aerosol OT, AOT)/isooctane reverse-micelle system[55,56](AOT from KISHIDA CHEMICAL Co.,Ltd.). The micelles contain the water-soluble PA OX063 trityl (from GE HealthCare), along with ^{13}C-labeled urea (from Cambridge Isotope Laboratories, Inc.) as the target molecule, and are suspended to the natural abundance isooctane, which serves as background molecules present in large amount.

Reverse micelle is a system with surfactant separating the polar phase and nonpolar phase. The volume of the polar phase is lower than that of the nonpolar phase, thus the reverse micelle system is an emulsion with the polar phase enclosed by surfactant, forming spherical reverse micelle that scattered in the nonpolar phase. The polar phase could constrain water-solvable polarization agent and the NMR signals from two types of substance exclusively dwell in polar phase or nonpolar phase with distinctive chemical shift could be used to monitor the DNP enhancement. Defining the space can be reached by DNP enhancement as the target space, then the space outside of the reach of DNP enhancement is the background space, signal from where is to be suppressed by the method. With different DNP build-up time, the reach of DNP enhancement may be larger, smaller or the same as the radius of the reverse micelle. Thus, by analyzing the change of signal intensity from the polar phase and nonpolar phase with different DNP build-up time, I can evaluate the reach of DNP enhancement and effectiveness of the background signal suppression.

The frequently used and intensely researched water/AOT/isooctane reverse micelle, with the modification of adding glycerol (60 vol%) and 2-butanol (30 vol%) to water and isooctane, respectively, is sufficient for the purpose. A model shows the composition of a reverse micelle is given in Figure 2.2.1. And Figure 2.2.2 shows the molecular structures of the chemicals used in the preparation of the reverse micelle sample. The natural abundance of ^{13}C from isooctane and 2-butanol, due to the large amount of existence in the sample, is adequate as the NMR signal sourced from nonpolar phase. The modifications of adding glycerol and 2-butanol are to suit the DNP-NMR experiment that is conducted with the sample frozen under cryogenic temperature. The whole sample, including both the polar solvent and nonpolar solvent is required to be frozen into vitreous, or glassy state. It is necessary for preventing the polarizing agent from aggregation and keep the structure of the reverse micelle intact. For the nonpolar solvent, isooctane alone transit into crystalline state after frozen with liquid nitrogen. After trials on several available chemicals, it is revealed that the mixed isooctane and 2-butanol in volume ratio 7:3 will transit into glassy state after frozen with liquid nitrogen. Further reducing the amount of 2-butanol in this mixture to, for example, volume ratio 8:2 will cause the mixture to transit into crystalline state after frozen. For the polar phase solvent, I used the 'DNP juice',[57] that is, mixed glycerol and water in volume ratio 6:4 to make sure it will be frozen into glassy state. The dual phase isooctane/2-butanol 7:3 and glycerol/water 6:4 mixture changes to single phase after the injection of AOT and vortex. This process has no visual difference with the case of the conventional water/AOT/isooctane reverse micelle, indicating that this modification does not have great effect on the formation of reverse micelle. The whole sample for the DNP-NMR experiment is tested that it indeed transits into glassy state after frozen with liquid nitrogen.

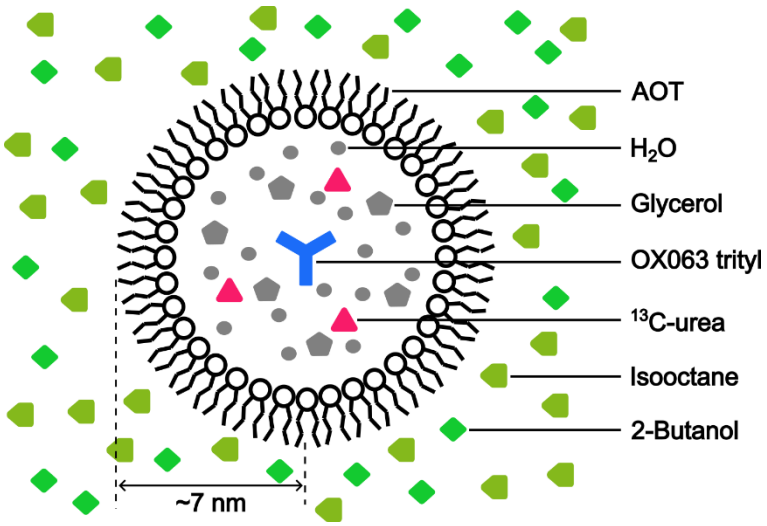

Figure 2.2.1 Schematic of the reverse-micelle system, emulating the PA delivered close to the target molecule (^{13}C-urea). The positions (inside or outside the reverse micelle) of each type of molecule used to prepare the reverse-micelle sample are represented in the figure.

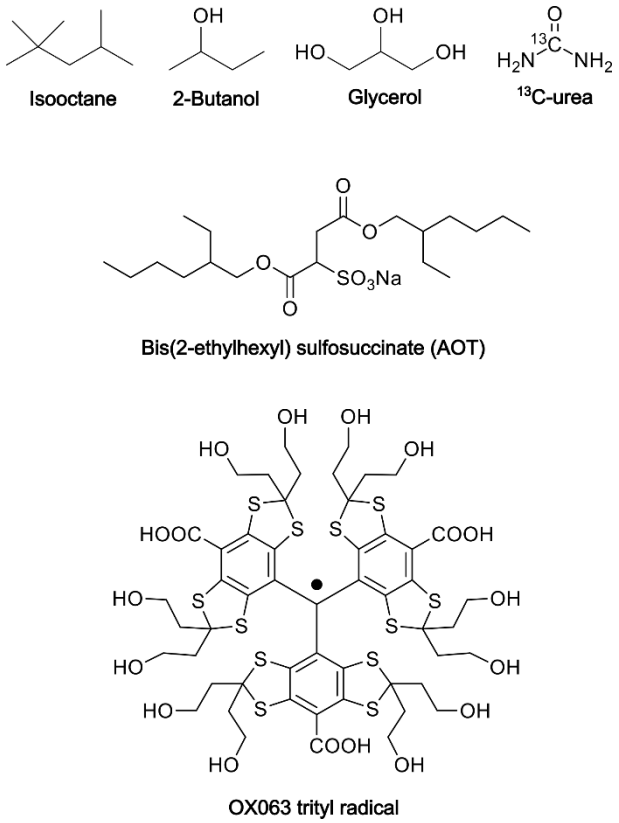

Figure 2.2.2 Molecular structures of the chemicals used in the preparation of the reverse-micelle sample.

A process of trial and error is adjusting the amount of nonpolar solvent, polar solvent and AOT to dissolve OX063 trityl in the reverse micelle emulsion, that is, adjusting the average size of the reverse micelle to contain OX063 trityl molecule inside. Luckily, the green color of OX063 trityl greatly reduces the labor in the adjustment. In the conventional water/AOT/isooctane reverse micelle system, the reverse micelle formed by water and AOT is relatively dilute in isooctane. The average size of the reverse micelle is directly indicated by the ratio, ω_0, of molar concentration of water and AOT, [water]/[AOT]. In the intensive experimental or simulation research on the size of reverse micelle, the ω_0 is usually below 20. However, in the experiment, an ω_0=20 reverse micelle system (The ω_0 is defined with the water replaced by the same volume of glycerol/water 6:4 solvent and the isooctane replaced by the same volume of isooctane/2-butanol 7:3 solvent) is clearly not large enough to contain OX063 trityl molecule as only very small amount of OX063 trityl can be dissolved. I increase the volume of glycerol/water 6:4 solvent to properly dissolve OX063 trityl. The solvability of OX063 trityl increases exponentially with the increment of water addition (Figure 2.2.3).

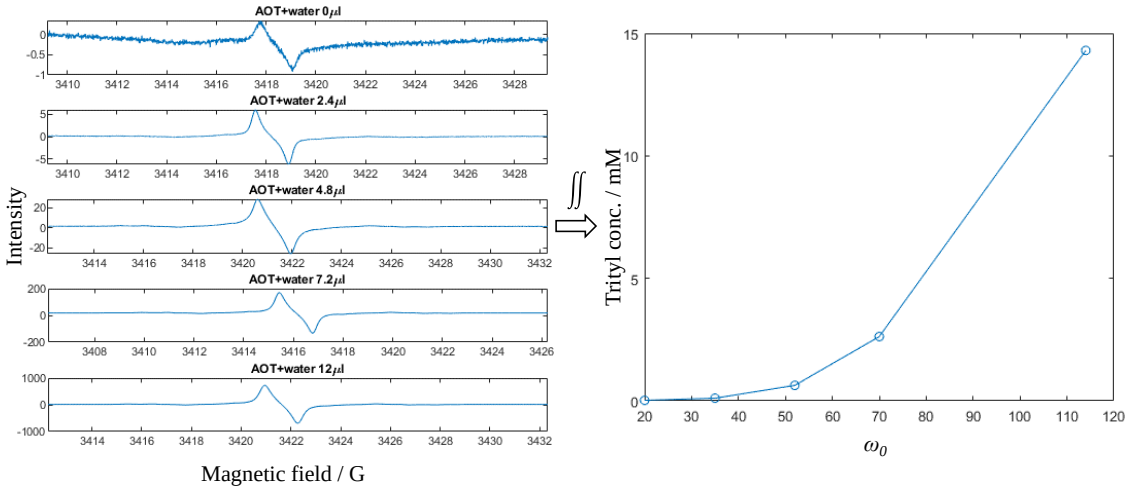

Figure 2.2.3 Solvability of OX063 trityl increases exponentially with the increment of water addition. The solution of 0.1M AOT, isooctane/2-butanol 7:3 (v/v) 100 μL and

glycerol/water 6:4 (v/v) 3.6 µL, which has a ω_0 = 20, shows almost no solvability of OX063 trityl. Additional 0, 2.4, 4.8, 7.2, 9.6 and 14.4 µL of water was added, saturated with OX063 trityl and the supernatant was measured with ESR. The signal of OX063 trityl in the ESR spectra was integrated twice, showing the OX063 trityl concentration increases exponentially with the increment of water addition (in the form of ω_0).

In the final sample, the ω_0 = 63.6. In this case I can have 16.3mM of OX063 trityl dissolved in the polar solvent, inside the reverse micelle, to make sure enough DNP enhancement could be induced. However, with an ω_0 this high and the complication of the reverse micelle system, it is possible that the phase of the emulsion has changed from reverse micelle to normal micelle or liquid crystal.[58,59] I indeed observed the visual sign of the possible co-existence of reverse micelle and normal micelle if the amount of AOT is not enough. With the adjustment of the amount of AOT, I managed to make the sample to be in a single homogeneous phase (Figure 2.2.4).

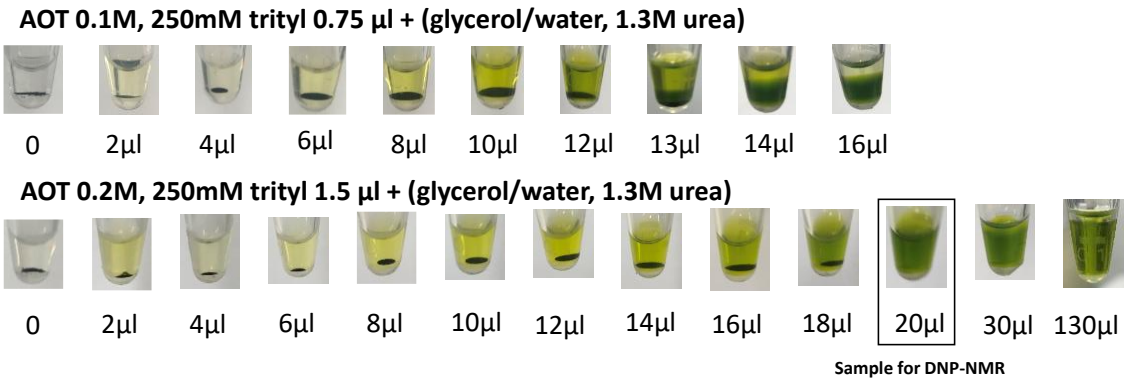

Figure 2.2.4 Adjust the amount of AOT and polar solvent to obtain a homogeneous sample for DNP-NMR experiments. Figures show the gradual solution of OX063 trityl with the addition of polar solvent. Several co-exist phases were observed during the process. The sample squared in the figure has a single homogeneous phase and was used for DNP-NMR experiments.

Thus, the preparation of reverse micelle sample is summarized as follows. First, AOT was lyophilized. Then, 250 mM OX063 trityl water solution (1.5 μL) was mixed into 0.25 M AOT isooctane/2-butanol (7:3, v/v) solution (80 μL). After the resultant mixture was vortexed and centrifuged (with tabletop mini centrifuge), solid OX063 trityl was found to be precipitated out. 1.3 M ^{13}C-urea glycerol/water (6:4, v/v) solution (0.5 μL) was then added repeatedly, with vortexing and centrifugation after each addition to observe the dissolution of OX063 trityl. A cumulative 21.5 μL of the ^{13}C-urea glycerol/water solution was added until a single homogeneous phase reverse-micelle sample was obtained without any precipitation.

The final composition of the sample included 80 μL of nonpolar solvent, 23 μL of polar solvent, 0.194 M AOT in the whole sample, 16.3 mM OX063 trityl and 1.22 M ^{13}C-urea in the polar solvent. That is, system contains 21 μmol ^{13}C-urea, 338 μmol isooctane and 261 μmol 2-butanol. Thus, the number of carbon spin in the background is about 133 times larger than that of the target, comparable to the low selectivity issue of ^{13}C in-cell NMR mentioned in the introduction. Here, the ^{13}C labelling of the urea lowers the ^{13}C ratio of background to target to 1.3 time, reflecting the case that target is selectively labelled.

I conducted electron-spin resonance (ESR) experiments to investigate the potential leakage of OX063 trityl. Given the weak mutual solubility between 2-butanol and water,[60] it was concerned that, if a small amount of water was present in the nonpolar phase of the reverse micelle system, the OX063 trityl might also exhibit weak solubility in that phase. To assess the potential leakage

of OX063 trityl, I conducted ESR experiments on an X-band ESR spectrometer (BRUKER ELEXSYS-II E500 CW-EPR) with a field sweep set at 20 G. The first spectrum was obtained from the sample used in the DNP-NMR experiments. For the second spectrum, I prepared a sample with identical components to the first but without AOT. This preparation resulted in phase separation, yielding a transparent supernatant and a lower phase in which a high concentration of OX063 trityl was visibly present. I then used the supernatant for the ESR measurement. The results are displayed in Figure 2.2.5. The ESR spectrum of the sample used in the DNP-NMR experiments showed a clear signal of OX063 trityl. By contrast, the ESR spectrum of the supernatant from the sample without AOT showed no OX063 trityl signal. Therefore, I concluded that OX063 trityl did not leak from the reverse micelle into the nonpolar phase.

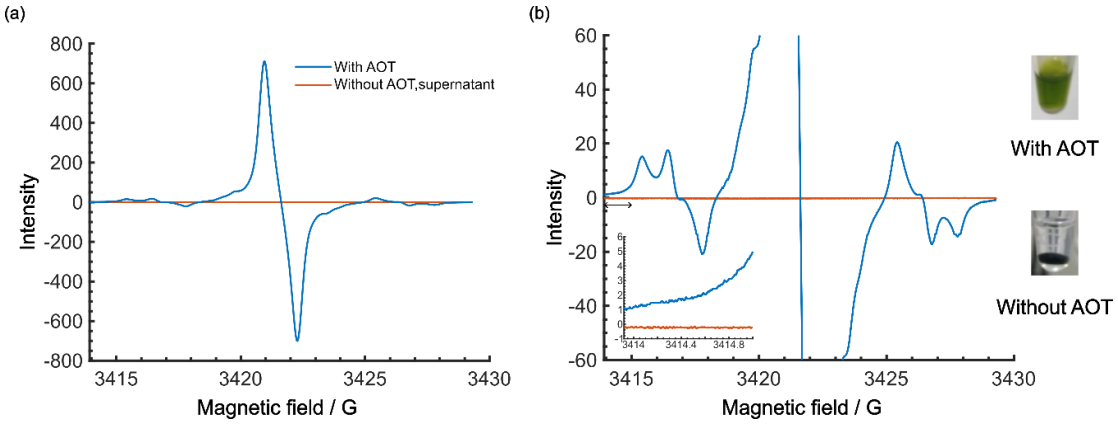

Figure 2.2.5 The ESR spectra for evaluating OX063 trityl leakage. (a) The blue spectrum was acquired for the sample from the DNP-NMR experiments, whereas the orange spectrum was acquired for the supernatant of a sample identical to the first but without AOT. The spectra in (a) are zoomed in vertically to (b), showing satellite peaks due to hyperfine interaction with natural abundance ^{13}C and ^{1}H. The inset in (b) further zoom in from 3413.92 to 3415 G, showing the noise level of the spectra. Photos of each sample are

provided adjacent to the spectra.

I used dynamic light scattering (DLS, DynaPro NanoStar, Wyatt Technology) to measure the size of the reverse micelles. Because of the color interference from OX063 trityl, I prepared a DLS sample that was identical to the one used in the DNP-NMR experiments but without OX063 trityl. I estimated that the viscosity of a mixture of isooctane and 2-butanol in a 7:3 volume ratio is very close to that of water,[61] enabling us to use the default value for the required solvent viscosity setting. The data was automatically processed in the machine. The results (Figure 2.2.6) reveal that the majority of the reverse micelles have a diameter of 14.2 nm, or a radius of 7.1 nm. Based on the expected micelle concentration, the separation between the micelles was ~28 nm on average (Supposing surface area of each AOT is 0.25 nm^2).[62]

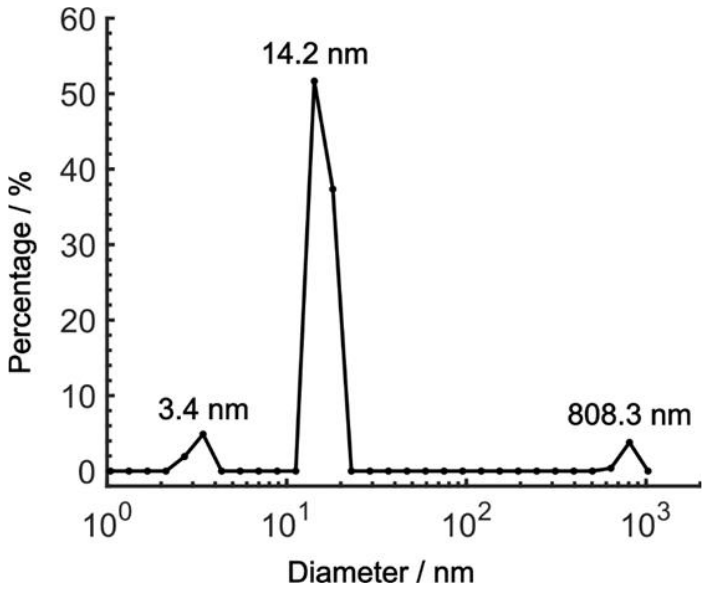

Figure 2.2.6 The DLS results for the reverse micelles. The curve shows the percentage distribution of the diameters of the reverse micelles. The diameters corresponding to each peak of the distribution are indicated in the figure.

Additionally, a nanodiamond sample is prepared to validate the Oops method. The

nanodiamond is a polarizing agent that the dangling bonds on surface of nanodiamond provides unpaired electrons. It is expected as potential PA for in-cell DNP-NMR due to the unpaired electrons will not be reduced in cytoplasm. The nanodiamond was scattered in natural abundance glycerol. Thus, with the MW irradiation, the ^{13}C spin inside the nanodiamond that is close to the dangling bonds will be DNP enhanced. While the ^{13}C spins of the glycerol that is scattered in the surrounding space of the nanodiamond only receive enhancement when their locations are reached by the spin diffusion propagating DNP enhancement. Thus, only a portion of them will receive DNP enhancement. The ^{13}C spin inside the nanodiamond can play the role of target, while the ^{13}C spins of the glycerol that are not DNP enhanced can play the role of background. This nanodiamond sample is difficult to reveal the full potential of the Oops method, as the ^{13}C spins of the glycerol that are very close to the surface of the nanodiamond will be DNP enhanced just as the ^{13}C spin inside the nanodiamond. Thus, the nanodiamond sample is intended only as a supplement for the validation.

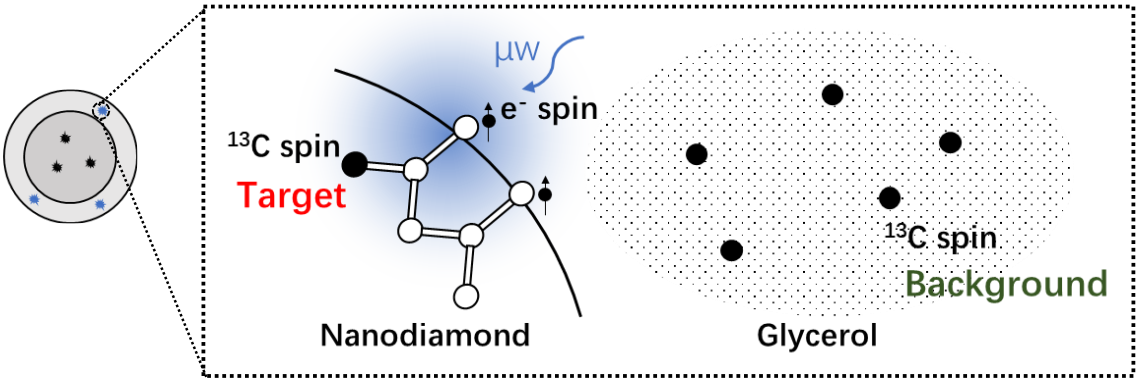

Figure 2.2.7 Schematic of the nanodiamond sample. The unpaired electrons of a nanodiamond, when irradiated by MW, will enhance the NMR signal of its adjacent ^{13}C spins in the nanodiamond, which are the target. For the ^{13}C spins in the glycerol scattered in the surrounding space, which are the background, only a portion of them will receive DNP enhancement.

2.3 DNP-NMR Experimental Methods

One of the simplest methods to experimentally demonstrate the efficacy of this method is by separately acquiring the spectra with positive and negative DNP experiments and then calculating the difference between them. For this approach, I used the pulse sequence shown in Figure 2.3.1. The MW source was continuously on, and its frequency was set to excite the positive or negative DNP. After the initial saturation pulses, polarization build-up/spin diffusion time (τ) was set before the data acquisition, which determines the range of the target space together with the spin diffusion rate *D*. For proof of principle, I experimentally demonstrated background suppression and its range of selection based on the direct ^{13}C-excitation DNP with ^{13}C–^{13}C spin diffusion and evaluated the results using simulations.

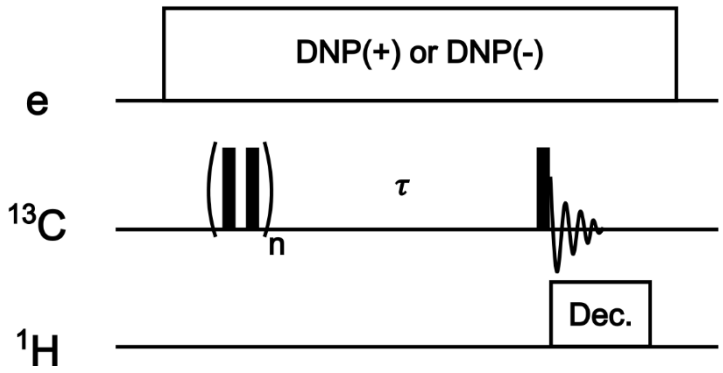

Figure 2.3.1 The pulse sequence for carrying out positive and negative DNP-NMR experiments.

^{13}C DNP-NMR experiments were conducted on a 16.4 T MAS NMR spectrometer (JEOL ECA-700II) equipped with a homemade 460 GHz gyrotron and a closed-cycle He MAS system.[63,64] The output power of the gyrotron was

~10 W. For these experiments, samples were placed inside a 3.2 mm MAS rotor, which was rotated at 7 kHz. The DNP-NMR experiments were conducted at 37 K, whereas the DNP-off NMR experiments were conducted at 28 K. Prior to each scan, to initialize the magnetization for both target and background, ^{13}C and ^{1}H spins were pre-saturated with a train of ~160° pulses, each lasting 10 μs, with a 10 ms interval between pulses. A series of DNP build-up times τ ranging from 0 to 20,000 s was used in the experiments. For acquisition, a 90° pulse with a duration of 7.63 μs was used; the ^{1}H spins were decoupled using a SPINAL64 decoupling sequence.[65] Two transients were added for each spectrum. The basic NMR data processing was performed using the JEOL Delta. The exponential window function (10 Hz) was applied prior the zero-filling (to 1024 complex points) and Fourier transformation. The Oops spectral editing and other analyses were performed using MATLAB (version R2023b, MathWorks, Natick, Massachusetts).

For the reverse micelle sample, to determine the microwave frequencies for positive and negative DNP and to clarify the DNP mechanism for the observed DNP enhancement, I recorded the DNP frequency profile (Figure 2.3.2). The data were acquired by scanning the microwave frequency around the electron resonance of OX063 trityl and recording the intensity of the main peak for ^{13}C-labeled urea. Because of the limited frequency range of our microwave source (a gyrotron), the negative enhancement peak is not fully captured in the profile. Nonetheless, the absolute value of the maximum negative enhancement is adequately close to that of the positive enhancement peak. On the basis of these results, I used CW-MW set to 459.80 GHz for positive DNP and 460.19 GHz for negative DNP. This limitation in the microwave frequency range also restricts the focus to ^{13}C DNP experiments. I note

that the frequency difference between the maximum positive and negative enhancement 390 MHz is approximately twice the ^{13}C Larmor frequency (~360 MHz). Thus, I deduced that the primary DNP mechanism in the experiments is the SE, similar to the recent report at 14.1 T and 100 K.[66] Given that the solid effect occurs in a two-spin system consisting of one electron spin and one nuclear spin, this result suggests that the majority of the reverse micelles contain no more than one OX063 trityl molecule.

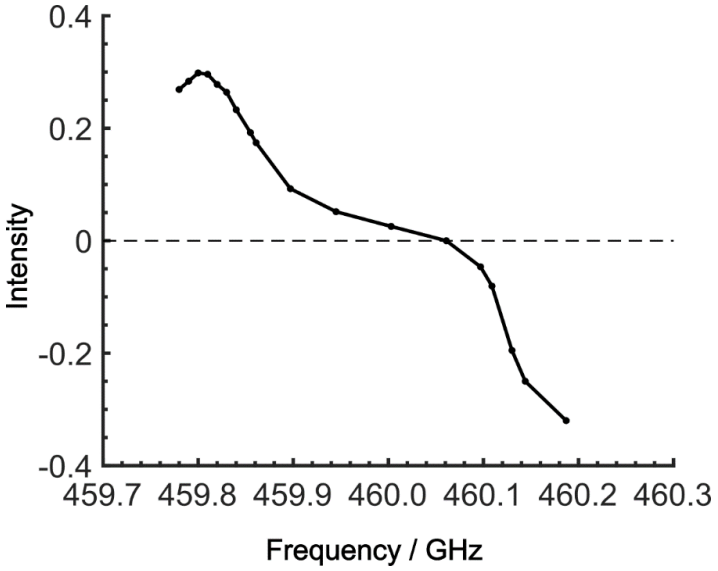

Figure 2.3.2 The OX063 trityl-induced ^{13}C DNP frequency profile. The horizontal dashed line at y = 0 is included as a guide.

For the nanodiamond sample, the CW-MW frequencies were determined in a similar manner. The CW-MW was set to 459.75 GHz for positive DNP and 460.00 GHz for negative DNP. The DNP frequency profile of nanodiamond is shown in Figure 2.3.3. The frequency difference between the maximum positive and negative enhancement 220 MHz is smaller than twice the ^{13}C Larmor frequency, indicating the primary DNP mechanism is CE or TM.

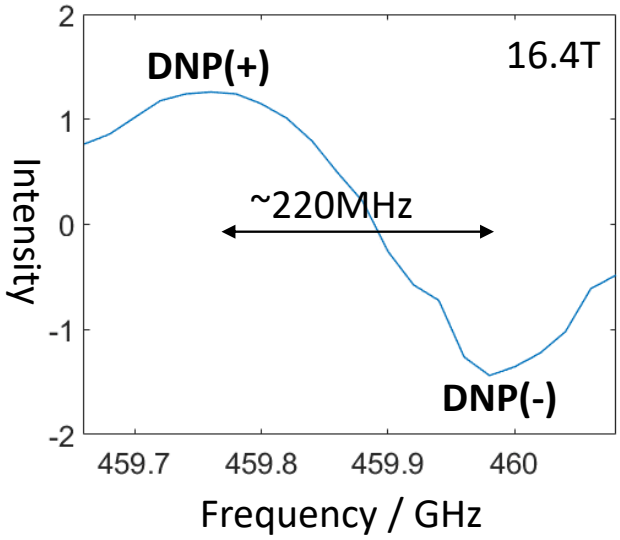

Figure 2.3.3 The nanodiamond-induced ^{13}C DNP frequency profile.

2.4 Experimental Results

For the reverse micelle sample, Figure 2.4.1 shows the direct-excitation ^{13}C NMR spectrum of the micelle sample collected at τ = 20,000 s ($\gtrsim 3T_1$ for both target and background) without MW irradiation (MW-off data). The assignment for each peak is shown in the spectrum.[67,68] The sample is suitable for validating the method because the peaks of the target (^{13}C-urea) and the background (isooctane/2-butanol) exhibit distinctive chemical shifts (Figure 2.4.1; regions indicated by dashed lines). To evaluate the efficacy of the background signal suppression, I defined a contrast factor as $C = I_T/I_B$, where I_T is the integral spectral intensity of the target (peak 12; integral from 146.7 to 186.7 ppm) and I_B is that of the background (peaks 3, 4, 6–8, 10, 11; integral from 1.6 to 41.6 ppm). The observed integral spectral intensities were [I_T, I_B, I_N] = [13.9, 24.9,

1.0] when normalized to the thermal noise intensity I_N (integral from 1.6 to 41.6 ppm at τ = 0). Thus, the contrast factor was very low, C = 0.56. This is consistent with the target to background number of ^{13}C spin ratio 1/1.3 = 0.77 calculated in the preparation of the sample. It shows that, with no bias toward the target, the background signals can seriously interfere with the target signal even if it is not isotopically labeled. The aim is to attain a higher contrast factor by selectively enhancing the target signal by DNP while suppressing the background signals.

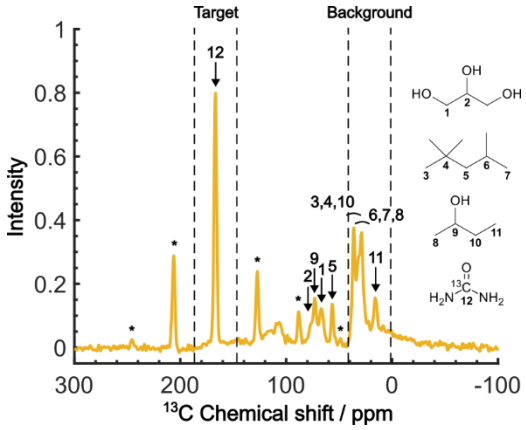

Figure 2.4.1 The MW-off ^{13}C NMR spectrum acquired at τ = 20,000 s, B_0 = 16.4 T, ν_R = 7 kHz and T = 28 K. The numbers assigned to each peak correspond to the carbon atoms in the molecular structures. Peaks marked with asterisks represent the spinning sidebands of the ^{13}C-urea peak. The peaks representing the target and background signals are indicated above the spectrum.

With the PA located in the micelles with the target molecules, applying DNP should increase the contrast factor. Figure 2.4.2a shows DNP-enhanced ^{13}C NMR spectra at τ = 20,000 s. Clear DNP enhancement was observed. The observed spectral intensities in the DNP conditions were [I_T, I_B, I_N] = [436.7, 135.4, 1.0] (for DNP+) and [394, 72.6, 1.0] (for DNP−) with the DNP enhancement of ε_T = 29.8 (for DNP+), −30 (for DNP−) and ε_B = 5.2 (for DNP+), −3.2 (for DNP−). With the trityl radical confined in

the reverse micelles, a much higher DNP enhancement was obtained for the target than for the background, which increased the contrast factor to C = 3.22 although I_B is still much higher than I_N.

I now consider how to improve the contrast factor further. Noting that the spins in the background experience finite negative DNP enhancement, it is evident that, at τ = 20,000 s, spin diffusion propagates the DNP enhancement to the space outside the reverse micelles. To reduce this leakage of hyperpolarization, the DNP build-up time could be reduced, thereby reducing the polarization propagating through spin diffusion. Assuming that the ^{13}C spin-diffusion rate is on the order of 0.01 nm^2/s, as estimated from the literature values[69–71] scaled by $D \propto \gamma^2 \sqrt[3]{[^{13}\mathrm{C}]}$,[72] the build-up time needs to be within ~100 s to confine the hyperpolarization to a few nanometers from the PA (i.e., within the micelles). Figure 2.4.2b shows the MW-on spectra acquired at τ = 60 s. Rather unexpectedly, however, the background peaks are still clearly visible, and the contrast factor C = 3.84 in this case did not substantially increase compared to the case where τ = 20,000 s (C = 3.22). This result is understandable given the sheer volume of the background that has a build-up rate similar to that of the target. Therefore, simply shortening the diffusion time τ is often ineffective for suppressing the background signal and it just adversely affects the S/N ratio for the target signal.

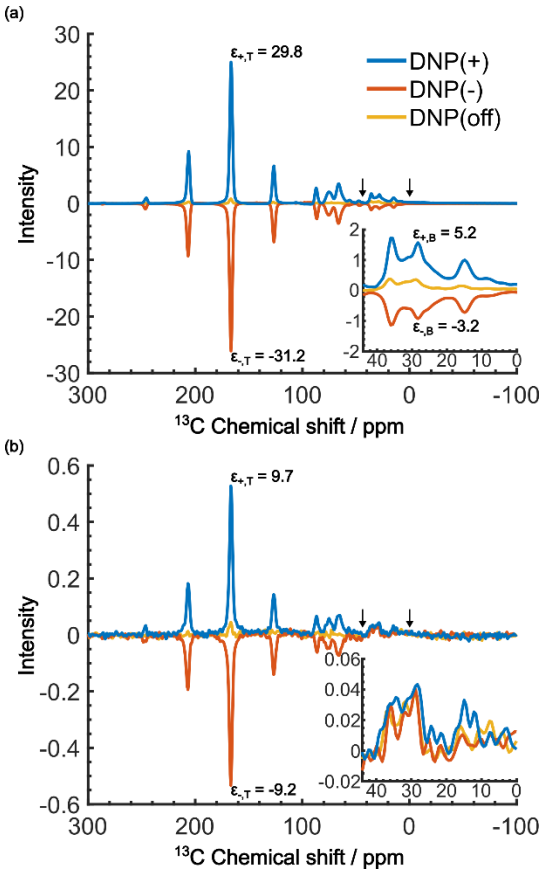

Figure 2.4.2 DNP-enhanced ^{13}C NMR spectra acquired at B_0 = 16.4 T, ν_R = 7 kHz, and T = 37 K. (a) The spectra for positive DNP (blue), negative DNP (red), and MW-off (yellow), all at τ = 20,000 s. (b) The same as in (a) but at τ = 60 s. The insets show enlargements of the background region between the two arrows (0 to 44 ppm). The DNP enhancements are shown in the spectra for the target and background signals.

Even in this situation, the Oops procedure enables a clean background signal suppression because, at τ = 60 s, the background signal shows similar positive intensity under both positive and negative DNP conditions (Figure 2.4.2b, inset), which will cancel each other. Figure 2.4.3c shows the results of the Oops treatment. The peaks representing the background signal are successfully suppressed to the noise level ([I_T, I_B, I_N] = [18.4, 1.43, 1.0]), increasing the contrast factor to C = 12.9. Compared with the MW-off data subtraction approach (Figure 2.4.3b; [I_T, I_B, I_N] = [11.2, 1.62, 1.0], C = 6.91), the method achieves 87% higher contrast factor in the

same total experimental time. These results validate the efficacy of the method relative to the conventional approaches for background signal suppression.

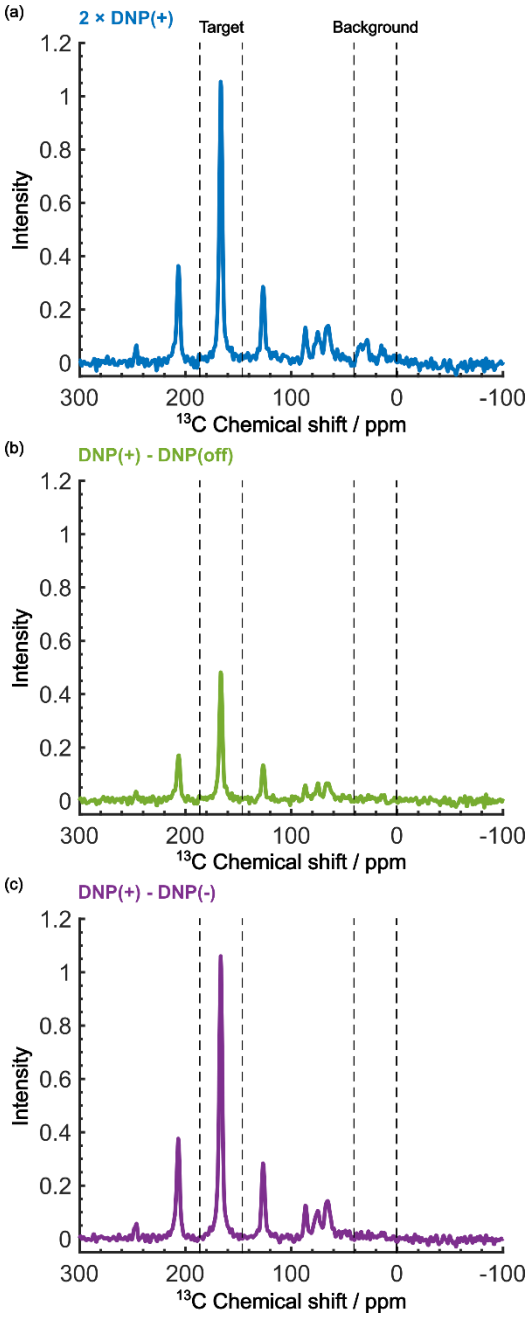

Figure 2.4.3 Demonstration of the background signal suppression at τ = 60 s. The DNP-enhanced spectra with (a) the positive DNP, (b) the MW-off data subtraction, and (c) the Oops treatment is shown. Data in (a) is the same as in Fig. 2.4.2b (blue) but was vertically scaled by a factor of 2 for direct comparability in the same total experimental time.

To overview the background signal suppression efficiency, it is plotted in Figure 2.4.4 the contrast factors against the build-up time. Each curve corresponds to the three distinct conditions described above: (i) conventional positive DNP, (ii) the MW-off data subtraction, and (iii) the Oops treatment. All the cases are displayed for the same total experimental time. Consistent with the observations described above, simply reducing the build-up time in the conventional positive DNP condition barely improves the contrast factor (blue data). Contrastingly, the Oops procedure improves the contrast factor at short τ (purple data), with C always being higher than that for the MW-off subtraction (green). Both cases (ii) and (iii) show contrast factors that first increase with τ, then decrease toward that for case (i), with a maximum at $\tau \sim$ 100 s. These results are qualitatively explained by the hyperpolarization not propagating to the background space before the maximum, whereas the target signal increases with increasing τ. After the maximum, the hyperpolarization propagates to the background space, which reduces the contrast. For the Oops treatment, the maximum contrast was $C = 12.9$, which is much higher than $C = 6.91$ for the MW-off subtraction and $C = 3.84$ for the conventional DNP.

Shortening τ controls the target range, and the Oops procedure maximizes the contrast factor; however, this approach inevitably reduces the S/N ratio for the target signal if τ is shorter than the polarization build-up time constant. To investigate this point, I also plotted the unit-time S/N ($SN/\sqrt{\tau}$) with dashed lines in Figure 2.4.4. The nearly identical $SN/\sqrt{\tau}$ traces for cases (i) and (iii) show that the decrease in $SN/\sqrt{\tau}$ is not due to the Oops procedure per se. At $\tau = 60$ s, where C is maximal, the $SN/\sqrt{\tau}$ for the target (~2.2) was approximately one-third of its maximum value (~6.4) at $\tau = 5000$ s. This result means that the background signal is suppressed at the expense of two-thirds of the unit-time sensitivity for the investigated micelle sample (purple) (other

cases are examined in the Discussion). By contrast, with conventional DNP, shortening the diffusion time gains no contrast but simply loses the sensitivity for the target (blue).

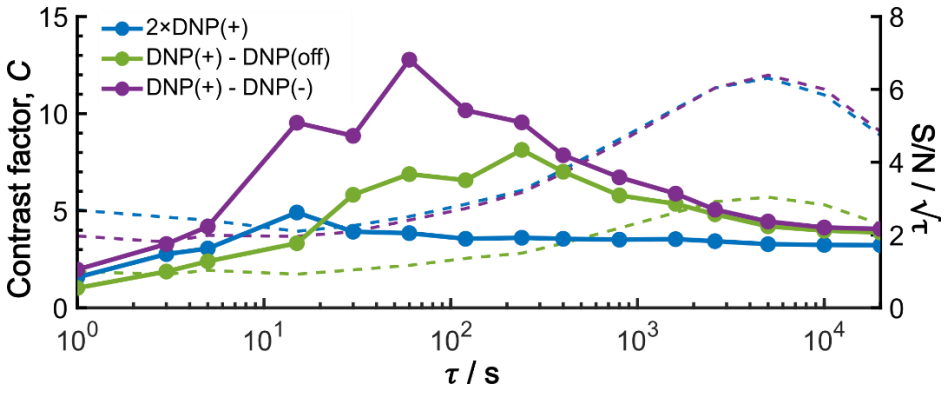

Figure 2.4.4 Build-up time dependence of the experimental contrast factor (dots and lines), and SN/τ (dashed lines; right axis), shown for the positive DNP (blue data), the MW-off data subtraction (green data), and the Oops treatment (purple data). To compare all the cases for the same total experimental time, the data for the conventional positive DNP taken with only two scans was multiplied by 2 for the S/N ratio calculation; the same noise intensity was used for all the data.

Additionally, the results of the Oops treatment on the nanodiamond sample is given in Figure 2.4.5. The target signal, from the nanodiamond ^{13}C spins adjacent to the unpaired electrons on the surface, shows positive intensity under both positive DNP and negative intensity under negative DNP, and with similar absolute intensity. While the background signal, from the ^{13}C spins from the glycerol, shows positive intensity under both positive and negative DNP conditions, but weaker intensity under negative DNP. This is expected as ^{13}C spins adjacent to the surface of nanodiamonds are also DNP enhanced. Even though, with the peak intensities represented by the height of peaks, the contrast factors *C* are calculated. And C=0.27 for the positive DNP

improves to C=0.70 after the Oops treatment, validating the effectiveness of the Oops method.

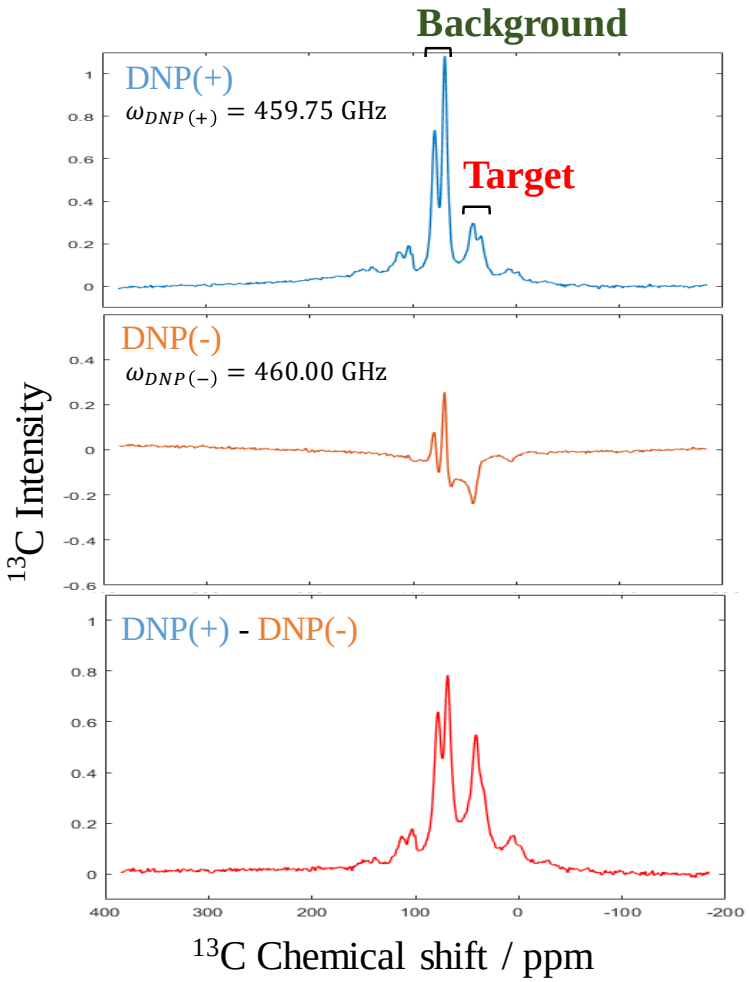

Figure 2.4.5 The background signal suppression for nanodiamond sample. Spectra with positive DNP, negative DNP and Oops treatment are shown. The peaks representing the target and background signals are indicated above the spectra.

2.5 Computational Methods and Results

As shown in Figure 2.4.4, the propagation of hyperpolarization into the not-of-interest/background region causes a decrease of the contrast factor. Therefore, the diffusion size should be carefully controlled to match the target to be selected. The

size of the target region depends on the spin diffusion rate, diffusion time, and the longitudinal spin relaxation rate. To understand more quantitatively how the polarization spreads in time and space, I built a classical one-dimensional spin diffusion model to fit the experimental polarization build-up curves. The analysis was conducted with the following equation, a classic one-dimensional diffusion equation (1) for the spin polarization $M(x,t)$ at a distance x from the PA and at time t:

$$\frac{\partial M(x,t)}{\partial t} = D_i \frac{\partial^2 M(x,t)}{\partial x^2} + R_{1,i}\left(M_{0,i} - M(x,t)\right) \quad (1)$$

I considered a thin polarization source (S) region (x = (0, x_S]) directly hyperpolarized by the PA (at x = 0), surrounded by the target (T) region (x = (x_S, x_T]) and then the background (B) region (x = (x_T, x_B]). Accordingly, Equation (1) has location-dependent parameters: the spin-diffusion rate D_i, the longitudinal relaxation rate $R_{1,i}$, and the equilibrium polarization $M_{0,i}$, where $i \in$ [S, T, B] (Figure 2.5.1).

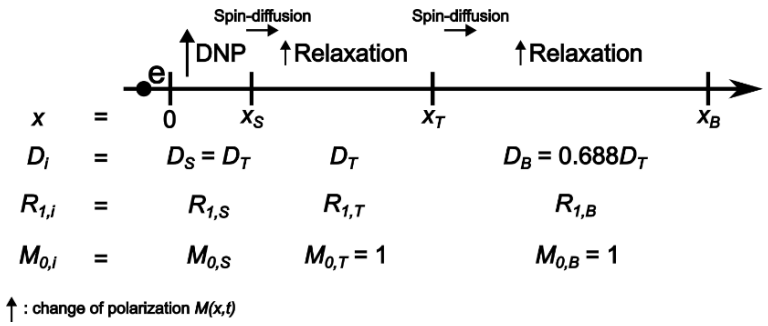

Figure 2.5.1 One-dimensional diffusion model with the parameters that require optimization. Distances that partition the model into three regions are marked on the diagram. The location-dependent parameters corresponding to each of these regions are shown in the figure. The mechanisms by which the polarization changes are also indicated in the figure.

In the source region, DNP drives the polarization toward $M_{0,S}$ for positive DNP conditions and toward $-M_{0,S}$ for negative DNP conditions with a rate $R_{1,S}$. The intrinsic spin relaxation rate here is absorbed into the DNP build-up process for simplicity. In the target and background regions, as well as in the source region when the MW source is off, the polarization relaxes toward the normalized thermal equilibrium value, $M_{0,S/T/B} = 1$, with the rate $R_{1,S} = R_{1,T}$ and $R_{1,B}$. The spin-diffusion rate in the T and B regions can be scaled to each other using the known ^{13}C density ρ_{13_C} for each region and the relation $D \sim \rho_{^{13}C}^{1/3}$. For the reverse-micelle sample described in the main text, $D_B = 0.688D_T$. The point x_T corresponds to the micelle radius and x_B corresponds to the midpoint between micelles. The equation is numerically solved using initial condition $M(x, 0) = 0$ and the Neumann boundary condition $\frac{\partial M(x,t)}{\partial t}|_{x=0,x_B} = 0$.

The parameters in the model were optimized to fit the following six experimental build-up curves globally: build-up of the height of the target (peak 12) and background (peaks 6/7/8), each taken under the DNP-off, DNP(+), and DNP(−) conditions. The parameters optimization was conducted using a simulated annealing module in MATLAB (version R2023b, MathWorks, Natick, Massachusetts). The fitting results were stable in the sense that repetition using random initial values yielded similar optimized parameters. The simulated time–space distribution of the polarization was separately integrated for the T and B regions for fitting the target and background peak build-ups.

As shown in Figure 2.5.2, the fitting result closely matches the observed build-up dynamics. For example, for the background build-up in the DNP(−) condition (Figure 2.5.2b, red), the intensity initially showed a small positive growth, then changed to a

large negative growth. This subtle feature was also reproduced in the model. This feature is attributed to the initial relaxation-induced background polarization being subsequently overwhelmed by the negative hyperpolarization relayed from the micelle. The parameters obtained in the optimization are summarized and compared with measured/estimated values in Table 1. All the values are close to the corresponding measured/estimated values, supporting the adequacy of the model.

Table 1 Parameters obtained by the model analysis compared with measured/estimated values.

Parameter	From fitting	Measured/ Estimated	Comment
x_S / nm	1.84	~3	Estimated from the e-^{13}C PRE distance
x_T / nm	6.43	~7	Micelle radius measured by DLS
x_B / nm	23.2	~14	Estimated from micelle concentration
$R_{1,S}$ / s^{-1} (R_{DNP})	1.1×10^{-5} (9.1×10^{4} s)	ND	–
$R_{1,T}$ / s^{-1}	1.3×10^{-4} (7.7×10^{3} s)	2×10^{-4} (5×10^{3} s)	Measured from the MW-off build-up
$R_{1,B}$ / s^{-1}	6.5×10^{-4} (1.5×10^{3} s)	7.1×10^{-4} (1.4×10^{3} s*)	Measured from the MW-off build-up
D_T / nm^2/s	0.011	0.01	Estimated from literature values
$M_{0,S}$	2650	2640	Estimated from the gamma ratio γ_e/γ_C

* The larger relaxation rate for ^{13}C spins outside the micelle is attributable to the large number of methyl groups in the isooctane and butanol.

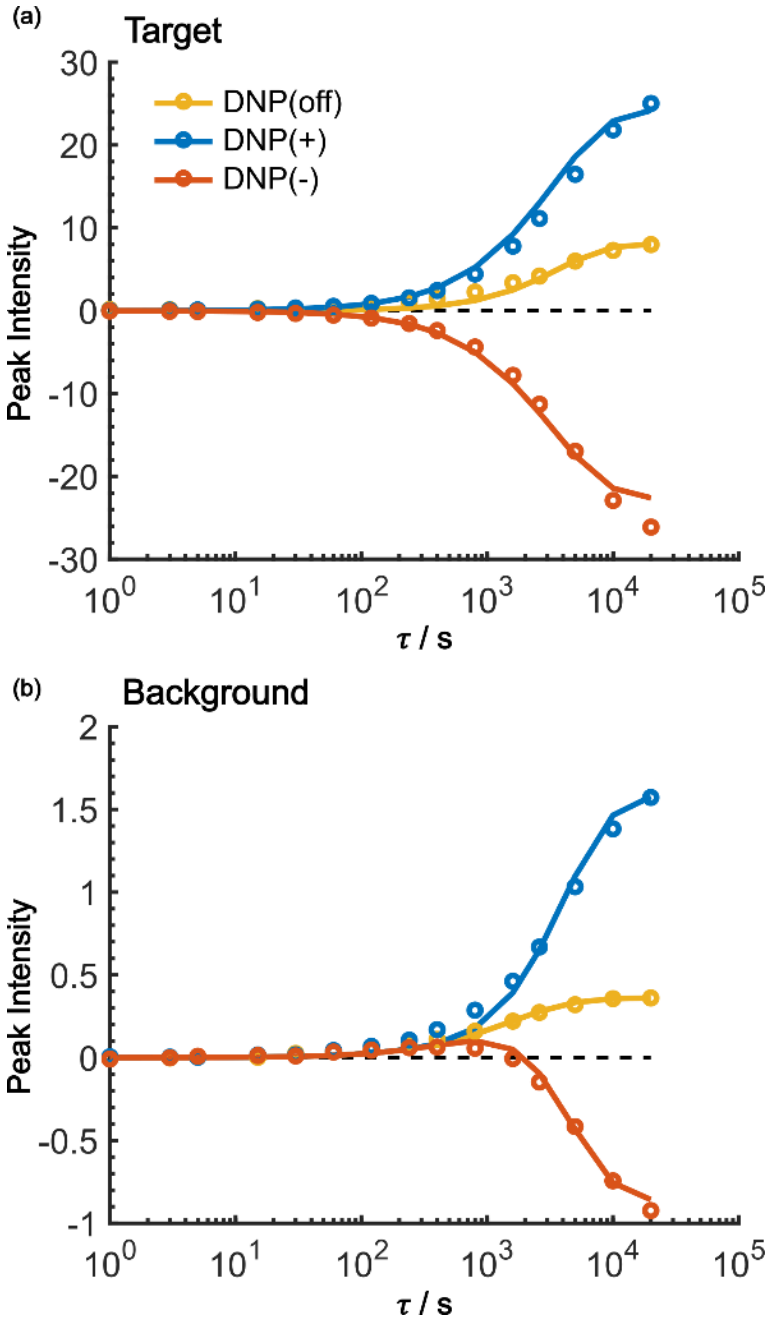

Figure 2.5.2 Fitting results of the build-up curves for the (a) target and (b) background peak build-up taken under the positive DNP (blue), negative DNP (red), and DNP-off (yellow) conditions. Circles are experimental data and lines are the model simulations. The values of the target signal under the DNP-off conditions are multiplied by 10 for visibility. In both panels, a horizontal dashed line shows $y = 0$.

Using the parameters obtained in the model study described above, I reproduced the space–time dependence of the polarization around the PA (Figure 2.5.3). In the plot, the polarization values were normalized by that at $x = 0$ for all τ to focus on the

polarization spatial distribution. Figure 2.5.3a and b shows the result for the standard positive DNP and that after the Oops procedure, respectively. In both cases, the distribution of the hyperpolarization around the PA remains largely unaltered, whereas in the case of the Oops procedure (Figure 2.5.3b), the relaxation-induced polarization outside the diffusion range is cleanly suppressed regardless of τ chosen. Thus, the target region is now simply determined by the diffusion time τ. Consistent with the aforementioned experiments, at $\tau \lesssim 100$ s, the size of the target region is indeed restricted to within ~3 nm from the PA, i.e., within the average radius of the micelle (with a ~1% drop-off criterion from the polarization at $x = 0$; refer to the dashed line labeled "0.01"). In the other extreme, at τ >10,000 s, target region as large as 18 nm can be selected (Figure 2.5.3b). With the ultra-low temperature we used in the present work (37 K), the ^{13}C longitudinal relaxation time typically exceeds ~1000 s even for the isooctane/butanol matrix with a high density of methyl groups and supports this long-range selection.

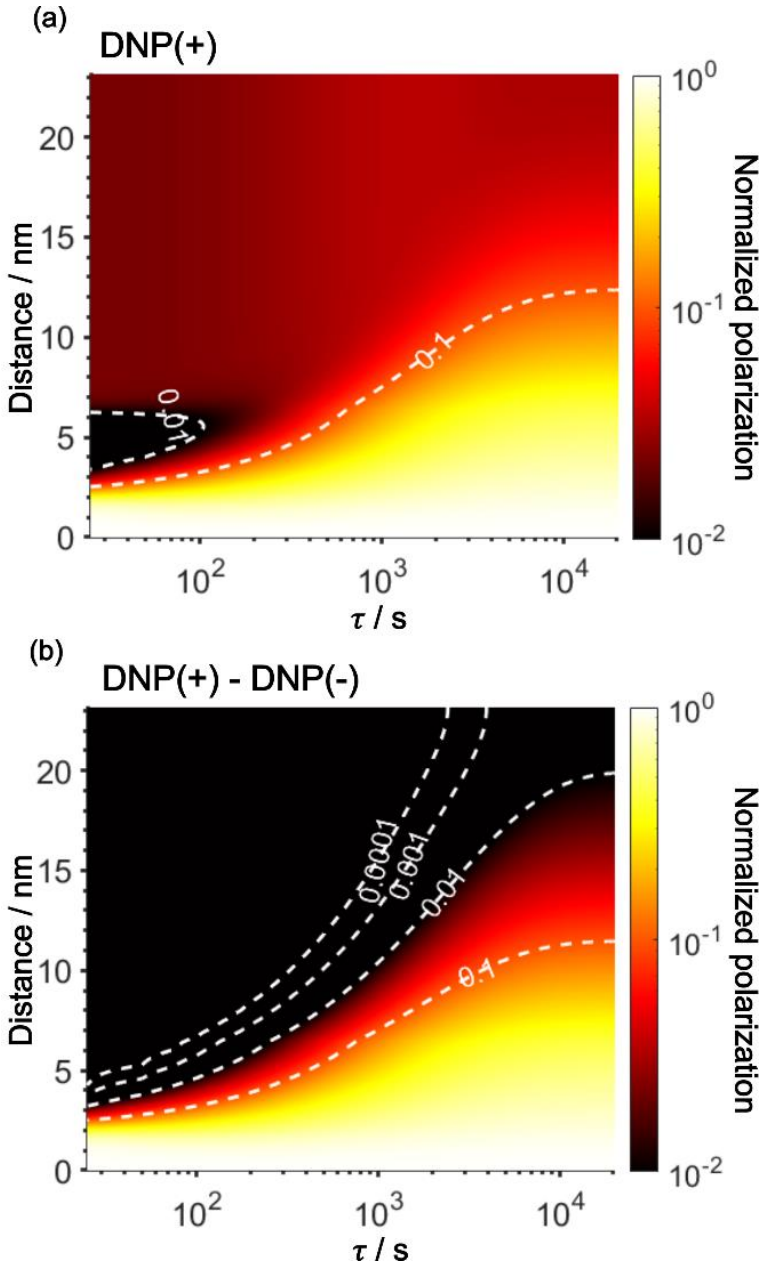

Figure 2.5.3 Simulated space–time distribution of the polarization around a PA. The polarization is normalized to that at $x = 0$ for all τ. Polarizations are shown for (a) a standard positive DNP and (b) the Oops DNP. The x-axis is in a logarithmic scale. The color of the heatmap is also scaled logarithmically. Labels with the contour lines indicate the polarization level.

2.6 Discussion

The space–time distribution of the hyperpolarization obtained from the analysis of the micelle data (Figure 2.5.3b) is not far from the result of an order-of-magnitude estimation based only on the typical ^{13}C diffusion rate (from D = 0.01 nm^2/s and $\sqrt{(Dt)}$): the hyperpolarization spreads to ~1 nm at 100 s and ~14 nm at 20,000 s from the PA. Even such a simple estimate can be useful in practical applications when choosing the diffusion time for target selection. When the sample's spectrum displays at least one distinguishable peak identifiable as the background signal, such as peaks of lipids or sugars separated from the target protein signals, τ can be empirically optimized in reference to the observability of these peaks. In addition, varying τ while monitoring the identity of the background signal would offer valuable information on the distance range for the background molecules from the PA. Note that such information is impossible to attain without the Oops treatment because, conventionally, relaxation-induced signals that have no distance dependence from the PA contaminate the observed spectrum.

Target selection by reducing the diffusion time comes at the expense of the S/N ratio for the target signal. In general, the smaller the target range, the greater the decrease in the S/N ratio. In the reverse-micelle case, where the selection of only a few nanometers from the PA was necessary, approximately two-thirds of SN/$\sqrt{\tau}$ was lost compared with that when the target signal was fully built. Still, the signal enhancement was on the order of 10 for the urea target in the reverse-micelle sample (Figure 2.4.2b), and the cost might be acceptable, especially when selectivity is critical. I also note that the signals from the MAS rotor materials (e.g., ^{27}Al in a sapphire rotor, ^{17}O in a ZrO_2 rotor, or ^{29}Si in a Si_3N_4 rotor) can always be removed

with the Oops treatment without adversely affecting the S/N ratio.

In this work based on ^{13}C spin diffusion, the method can potentially target molecules or moieties that are within ~2 nm to ~15 nm of the PA. This target range might enable individual molecular entities such as a protein fibril, a membrane protein assembly, or a thin functional layer on polymers/films to be targeted. To compare the performance of the Oops treatment in various other potential applications, I simulated the space–time dependence of the contrast factor by altering some of the parameters used in the model I established above. The simulated space–time dependence of the polarization at a given build-up time τ was integrated from 0 to x_{T} as the target signal intensity and integrated from x_{T} to x_{B} as the background signal intensity. The target and background signal intensities post-application of the MW-off subtraction and the Oops treatment, DNP(+) − DNP(off) and DNP(+) − DNP(-), were calculated. To align the simulation to experiments, the target signal intensity of the sample was further scaled by a constant $k_{\mathrm{t}} = 0.90$, and the background signal intensity was scaled by $k_{\mathrm{b}} = 0.71$. This scaling ensures that the calculated values at τ = 20,000 s after the application of DNP(+) − DNP(-) were equal to their corresponding experimental counterparts. The difference between the constants k_{t} and k_{b} can account for the experimental details not included in the model, such as the difference in the concentration of ^{13}C spins inside and outside the reverse micelles. After this process, the noise level in the simulation was designated as the experimental background signal intensity at τ = 0 s post-application of the Oops treatment. In the simulation of contrast factor with altered parameters, the noise level was kept the same for simplicity. Because the signal intensity for the experimental calculation of the contrast factor is the integral of the absolute value around the target or background peaks post-application of background signal suppression, the standard deviation of noise is

derived as $\sigma = \text{noise} * \sqrt{(\pi/2)}$. To represent the effect in the simulation where very small signal intensities are elevated to the noise level while large signal intensities remain unaffected, the noise-adjusted signal intensity was calculated as $S_\text{n} = F(S, \sigma)$, where F is the expectation value for the absolute integral of the white noise and S is the aforementioned signal intensity (equation (2)).

$$F(S,\sigma) = \frac{1}{\sqrt{2\pi}\sigma}\int_{-\infty}^{+\infty}|x|exp\left(-\frac{(x-S)^2}{2\sigma^2}\right)dx$$

$$= \sqrt{\frac{2}{\pi}}\sigma \cdot exp\left(-\frac{S^2}{2\sigma^2}\right) - S \cdot erf\left(-\frac{S}{\sqrt{2}\sigma}\right) \qquad (2)$$

Figure 2.6.1a shows the simulated dependence with the parameters optimized for the micelle sample with ^{13}C diffusion, where the set of relevant parameters is $\mathcal{P}$ = [D, R_T, R_B, x_T, x_B] = [0.01 nm^2/s, 1e^{-4} s^{-1}, 7e^{-4} s^{-1}, 6 nm, 23 nm] (Table 1). The space–time dependence qualitatively reproduced the experimental result in Figure 2.4.4 despite a right-shifted maximum and generally overestimated C. This discrepancy most likely be accounted for by the fact that the sizes of the target and background in the model are averaged values of the distribution of sizes of reverse micelles and their distance in actual samples. Concerning the size of the reverse micelles, the smaller ones influence the shape of the build-up of the contrast factor more strongly than the larger ones. Figure 2.6.2 shows the simulated build-up of the contrast factor with a distribution of x_T. Each panel has the same mean value of $\overline{x_T} = 6.43$ nm but a gradually broader distribution. Panel (a) shows the average results of five simulations, each with $x_T = 4.43, 5.43, \ldots 8.43$ nm, panel (b) shows the average results of nine simulations, each with $x_T = 2.43, 3.43, \ldots 10.43$ nm, and panel (c) shows the average

results of thirteen simulations, each with $x_T = 0.43, 1.43, \ldots 12.43$ nm. The optimal build-up time is clearly left-shifted, and the values of the contrast factor are lowered by the broader distribution of x_T, similar to the experimental results in Figure 2.4.4. Note, however, that the exact distribution of parameters can be underdetermined when extracted from the experimental data by fitting and optimization. Given that it is interested in the effect of parameter changes, I continue with this level of accuracy to examine other related cases in the following text.

As previously mentioned, selecting a larger target is easier. Figure 2.6.1b shows the case for $2x_{\mathrm{T}}$ ($\mathcal{P}$ = [0.01, 1e^{-4}, 7e^{-4}, **12**, 23], varied parameter is shown in bold). This corresponds e.g., to a twice-larger target micelle or twice-thicker polymer coating. As expected, the maximum of *C* occurs at a longer diffusion time because of the larger target. Also, the best contrast factor (C ~ 220) and corresponding unit-time sensitivity (SN/$\sqrt{\tau}$ ~ 7) were approximately three times and two times higher, respectively, than those in Figure 2.6.1a (C ~ 70 and SN/$\sqrt{\tau}$ ~ 4). Only ~30% loss of the SN/$\sqrt{\tau}$ relative to the fully built target was required to maximize *C*.

Figure 2.6.1c shows a plot of the result for a larger background, $10x_{\mathrm{B}}$ ($\mathcal{P}$ = [0.01, 1e^{-4}, 7e^{-4}, 6, **230**]). This scenario occurs, e.g., when the target proteins are diluted in a larger cell or a given surface coating is deposited onto a thicker base film. In this case, only the conventional positive DNP (blue) exhibited a substantially lower contrast factor; by contrast the result was not affected by the off-data subtraction (green) or Oops treatment (purple). These results demonstrate that the Oops background suppression maintains the best efficacy that is, in principle, impervious to the size of the background. This result is reasonable because the space–time dependence of the hyperpolarization around the PA is nearly unaffected by the definition of the

background size (Figure 2.6.1a2, b2, and c2).

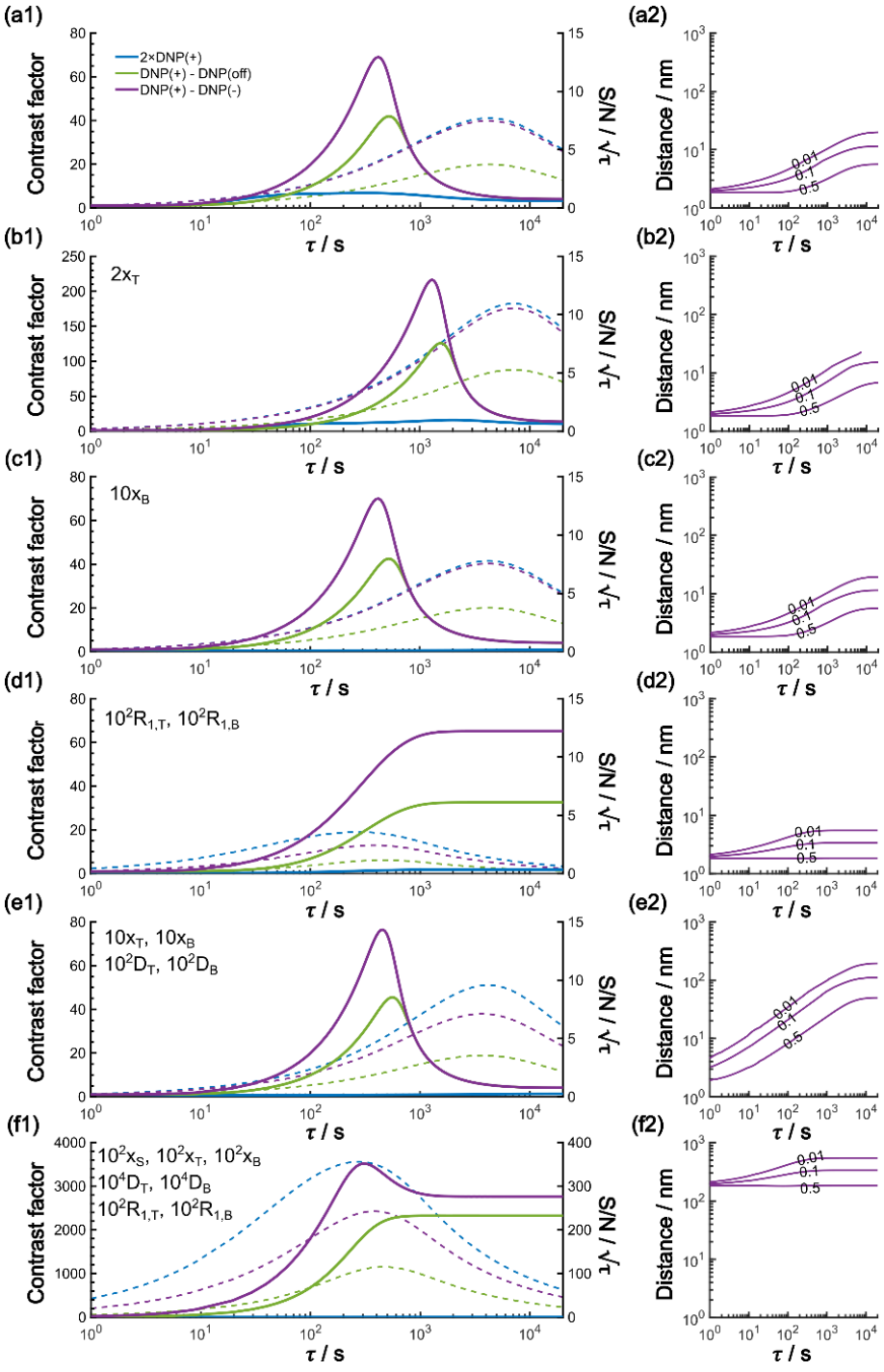

Figure 2.6.1 (a1−f1) Simulated τ-dependence of the contrast factor and (a2−f2) the polarization spatial distribution. In the latter, the polarization is normalized to that at x = 0 for all τ. In a1−f1, the SN/$\sqrt{\tau}$ is also shown by the dashed lines (right y-axis). (a) The results simulated using the parameters optimized for the experimental micelle data shown in the Results. (b–f) Varied parameter(s) is (are) indicated with the other parameters kept invariant: (b) target size is enlarged; (c) background size is enlarged; (d) the relaxation rate is elevated; (e) the target and background size, together with the

diffusion rate, are increased. (f) Combination of panels (d) and (e), showing that relaxation rates as well as the distance range and the diffusion rate all up-regulated.

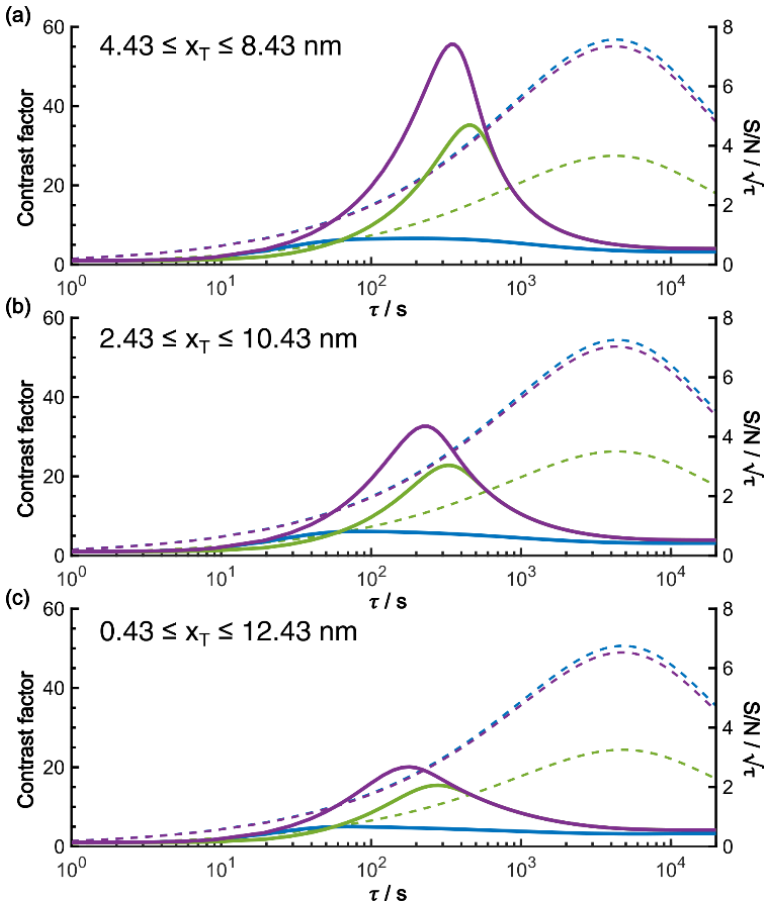

Figure 2.6.2 Simulated build-up of the contrast factor with a distribution of x_T. The distributions of x_T are given in each panel. Other conditions of the simulation and the color order of plotting are the same as in figure 2.6.1a1.

The spin relaxation rate is a strong function of the type of nuclear species, molecular structure, temperature, and the magnetic field strength and is a major factor that changes the space–time dependence of the contrast factor. Figure 2.6.1d shows results simulated for $100R_{T/B}$ ($\mathcal{P}$ = [0.01, $\mathbf{1e^{-2}}$, $\mathbf{7e^{-2}}$, 6, 23]). Because of the strong sinking effect for the hyperpolarization, the S/N ratio for the target was reduced substantially. Interestingly, however, the contrast factor remained high, similar to the case in Figure

2.6.1a, and reached a constant value at τ > 1000 s. This result is attributable to the rapid relaxation curtailing the polarization propagation and thereby alleviating the leakage of polarization beyond x_T = 6 nm. Indeed, the spatial distribution also remains constant at τ > 1000 s (Figure 2.6.1d2), which is a manifestation of the intrinsic targeting set by the balance between the diffusion and relaxation rates. When the size of the target matches the intrinsic range, the longer-than-optimal diffusion time τ is not a concern; only a slow loss of SN/$\sqrt{\tau}$ needs to be considered.

The spin diffusion rate also strongly varies depending on the nuclear spin species (gyromagnetic ratio) and its concentration. Slow spin diffusion among various low-γ nuclei (e.g., ^{31}P, $^{6/7}$Li, ^{29}Si, ^{113}Cd, and ^{119}Sn) has been used to show that the hyperpolarization can relay from the surface to the bulk supported by their long longitudinal relaxation time.[73,74] In such cases, the spin diffusion rate was often on the order of D ~ 1.0 or more under MAS, being at least ~100-fold higher than the micelle sample (D ~ 0.01 nm^2/s), and the characteristic diffusion length was ~100 nm. [35,36] Figure 2.6.1e1 shows the results for 100D and 10$x_{T/B}$ (the size of the source region x_S was fixed such that [**1.0**, 1e^{-4}, 7e^{-4}, **60**, **230**]). The behavior of the contrast factor is similar to that observed in figure 2.6.1a, which is understandable given that it should be invariant with a 10-fold scaling of the distance parameters, x_S, x_T, x_B (nm) together with a 100-fold scaling of the spin diffusion rate D_T, D_B (nm^2/s). However, the plot in figure 2.6.1e2 reveals that the target range is substantially enlarged, reaching ~200 nm at maximum, consistent with the diffusion length observed for the impregnated solid particles.[73,74] An advantage of the Oops technique is that it allows selective observation of the surface signals even when they are overlapped with those of the bulk matrix; in addition, the size of the observable target from the surface can be controlled between 5 and 200 nm in this example by varying the diffusion time.

Furthermore, the observed surface signals are at least partly enhanced by DNP, in contrast to the previously reported "surface-only spectroscopy," which relies on the observation of the two-spin order for the spatial selectivity, not on direct observation of the DNP-enhanced NMR signals.[75]

When the size of the target substantially exceeds ~100 nm, the Oops technique combined with ^{1}H spin diffusion might become useful either through direct ^{1}H or ^{13}C NMR through $\{^{1}H\}$–^{13}C cross polarization (CP). Diffusion among high-γ spins (such as ^{1}H and ^{19}F) is generally characterized by a high diffusion rate as well as a high relaxation rate. For example, the typical ^{1}H spin-diffusion rate in organic substances is approximately four to five orders of magnitude greater than that for ^{13}C, and the relaxation time T_{1H} is on the order of 10 s at 30 K. Figure 2.6.1f shows the results for 10,000D, 100$R_{T/B}$, and 100$x_{S/T/B}$ ($\mathcal{P}$ = [**100**, **1e**$^{-2}$, **7e**$^{-2}$, **600**, **2300**]). The behavior resembles that in Figure 2.6.1d, where the contrast factor reaches a constant value at long diffusion times although the targeted space is ~100-fold larger, becoming on the order of several hundred nanometers to 1 μm. This target range might be useful for selecting, e.g., whole-aggregation foci (~0.5 μm) or nucleoli (~1 μm) in eukaryotic cells (~10 μm).

The Oops background suppression can, in principle, be incorporated into multi-dimensional NMR experiments when the required τ is reasonably short relative to the total acquisition time. However, given the finite instrumental stability (such as the temperature, MAS rate, and MW output power), the interval between positive and negative DNP excitations should be as short as possible for an exact cancellation of the background signals. If the measurement is based on the ^{1}H spin diffusion, this interval is of less concern; however, for the long low-γ spin diffusion, separately

recorded two 2D datasets under DNP(+) and DNP(−) conditions for the subtraction would not be recommended. To address this issue, I propose a modified method incorporating the Oops treatment directly in the polarization build-up time period (Figure 2.6.3a). The positive and negative DNP are excited sequentially in a pulsed manner (with a duration τ_0) with a 180° pulse on the nuclear spin placed in-between. In the target space next to the PA, the hyperpolarization in the opposite polarities is accumulated because of the polarization-inversion 180° pulse. By contrast, in the background space, the polarization arising from the spin relaxation is consistently saturated by the series of 180° pulses. The size of the target region is still determined by the total DNP build-up time τ. Figure 2.6.3b and c show an example simulated using the parameters in Table 1 and with n = 7 and 20. As intended, the target intensity steadily increases with the polarization inversions, whereas the background intensity is gradually saturated (to less than ~1% of the target). The efficacy of background suppression slightly improves with the number of repetitions $n = \tau/(2\tau_0)$ but does not show a large change (i.e., not sensitive to the choice of n). Implementing this polarization inversion in experiments, however, requires a frequency-agile microwave source. The double-gyrotron setup is one possibility.[76]

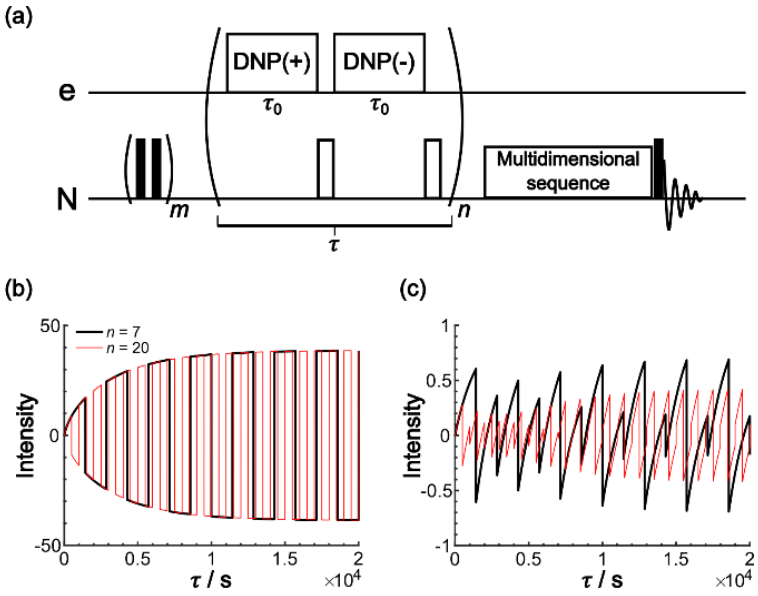

Figure 2.6.3 (a) Pulse sequence proposed for incorporating the Oops background suppression in the polarization build-up time period. Each DNP block is carried out for τ_0. The DNP(+), 180°, DNP(-), 180° pulses are repeated n times for a total time τ. The simulated build-up of the (a) target and (b) background signal intensity is shown. The signal intensity is simulated with the parameters in Table 1 and with $n = 7$ (black) and 20 (red). The target signal intensity is represented as the value at $x = 0$, and the background signal intensity is represented as the value at $x = x_{\mathrm{B}}$.

3. Improving DNP Efficiency

3.1 Methodology of Spin Dynamic Simulation

This section investigates the potential application of multi-frequency MW to enhance DNP efficiency through numerical simulations. The DNP enhancement frequency profiles were simulated under various scenarios, including several multi-frequency MW techniques and sample types. The experimental validation of the simulated results requires the double gyrotron or the solid-state MW source. Due to these MW sources being under maintenance or development, the focus here is only on the simulation aspect of this study.

The spin dynamic simulations were carried out using Spinach in MATLAB. Spinach is a third-party, open-source library of MATLAB designed for simulating NMR, ESR, DNP, etc.[77–80] In the research, Spinach's simulation of DNP and ESR uses the Liouville space formalism, with the master equation in the form $\partial/\partial \mathrm{t}\,\boldsymbol{\rho}(t) = (-\mathrm{i}\boldsymbol{H} + \boldsymbol{R})\boldsymbol{\rho}(t)$. Here, the Liouvillian $\boldsymbol{L} = -\mathrm{i}\boldsymbol{H} + \boldsymbol{R}$ combines the Hamiltonian $\boldsymbol{H}$ with the relaxation superoperator $\boldsymbol{R}$. The Hamiltonian $\boldsymbol{H}$ in the simulation of this dissertation, considering the Zeeman interaction of electron spin $\boldsymbol{H}_{\mathbf{e_{Zeeman}}}$ and nuclear spin $\boldsymbol{H}_{\mathbf{n_{Zeeman}}}$, zero-field splitting $\boldsymbol{H}_{\mathbf{ZFS}}$, hyperfine interaction $\boldsymbol{H}_{\mathbf{hyperfine}}$ and MW $\boldsymbol{H}_{\mathbf{MW}}$ can be generally given as:

$$\boldsymbol{H} = \boldsymbol{H}_{\mathbf{e_{Zeeman}}} + \boldsymbol{H}_{\mathbf{n_{Zeeman}}} + \boldsymbol{H}_{\mathbf{ZFS}} + \boldsymbol{H}_{\mathbf{hyperfine}} + \boldsymbol{H}_{\mathbf{MW}} \tag{3}$$

And each Hamiltonian can be further expressed as:

$$\begin{aligned} \boldsymbol{H}_{\mathbf{e_{Zeeman}}} &= \mu_B \boldsymbol{B_0 g S} \\ \boldsymbol{H}_{\mathbf{n_{Zeeman}}} &= \gamma_n \hbar \boldsymbol{B_0 I} \end{aligned} \tag{4}$$

$$\boldsymbol{H_{ZFS}} = \boldsymbol{SDS}$$

$$\boldsymbol{H_{hyperfine}} = \boldsymbol{SAI}$$

$$\boldsymbol{H_{MW}} = \mu_B \boldsymbol{B_1 g S} \cos(\omega_{MW_0} t)$$

Where μ_B is Bohr magneton, $\boldsymbol{B_0}$ is external magnetic field, $\boldsymbol{g}$ is electron g-tensor, $\boldsymbol{S}$ is electron spin angular momentum operator, γ_n is gyromagnetic ratio of nuclear spin, $\hbar$ is reduced Planck constant, $\boldsymbol{I}$ is nuclear spin angular momentum operator, $\boldsymbol{D}$ is electron zero field splitting tensor, $\boldsymbol{A}$ is hyperfine coupling tensor, $\boldsymbol{B_1}$ is MW magnetic field and ω_{MW_0} is MW angular frequency.

The density vector $\boldsymbol{\rho}(t)$ employs Irreducible spherical tensors as its basis set. Notably, the size of the Liouvillian scales by the fourth power of the number of spins. The simulation propagates the spin system using a time independent Liouvillian, $\boldsymbol{\rho}(t) = \exp(-\mathrm{i}\boldsymbol{L}t)\, \boldsymbol{\rho}(0)$.

For the simulation of MAS in solid-state DNP-NMR, the Liouvillian is time-dependent during one rotor period t_r. The propagator during one rotor period t_r is calculated in a stepwise fashion, with each step lasting t_r/N, (N is set to 4001 and $t_r/N \approx$ 2.5e-8 s in this dissertation) during which the Liouvillian is approximately time independent. The overall propagator for one rotor period is the product of each step's propagator. The effective Hamiltonian of one rotor period can be calculated from its propagator. Then, the spin system can be propagated to arbitrary number of rotor period using the effective Hamiltonian. For ESR simulations, full time-domain simulations were performed. For DNP simulations, nuclear spin magnetization $\boldsymbol{I_z} \cdot \boldsymbol{\rho}(t)$ was directly used to get the nuclear spin DNP enhancement.

3.2 Simulation Results: General Solid-Effect DNP under MAS

Considering the anisotropic part of the hyperfine interaction and *g* tensor changes with different orientations in a powder sample, causing the DNP matching frequencies to have a distribution. Thus, unlike conventional DNP which apply CW MW on a single frequency, a MW irradiation on a wider range is expected to yield higher DNP enhancement. As mentioned in section 1.3, I found that multi-frequency MW such as chirped MW was reported to improve the DNP efficiency for SE-DNP for static sample. While under MAS, DNP matching frequencies will fluctuate during DNP experiments. It occurred that using multi-frequency MW for SE-DNP under MAS for better DNP efficiency hadn't been reported yet. Thus, I explored possible applications of chirped MW for SE-DNP under MAS.

The simulation starts with one electron spin (S=1/2). I set the *g* tensor of the electron spin to be an arbitrary typical value [2.0014, 2.0016, 2.0039] (Similar to nitroxide radical such as TEMPO that has high anisotropic *g* tensor). Other parameters were set as magnetic field B_0 = 9.4 T (Considering solid-state MW source is not available under very high B_0, ours is connected to 9.4 T NMR), temperature T = 80 K (temperature is for the calculation of initial state density vector). The simulated ESR spectrum of the electron spin is shown in Figure 3.2.1. The rather anisotropic *g* tensor is expected to be more likely to benefit from the chirped MW.

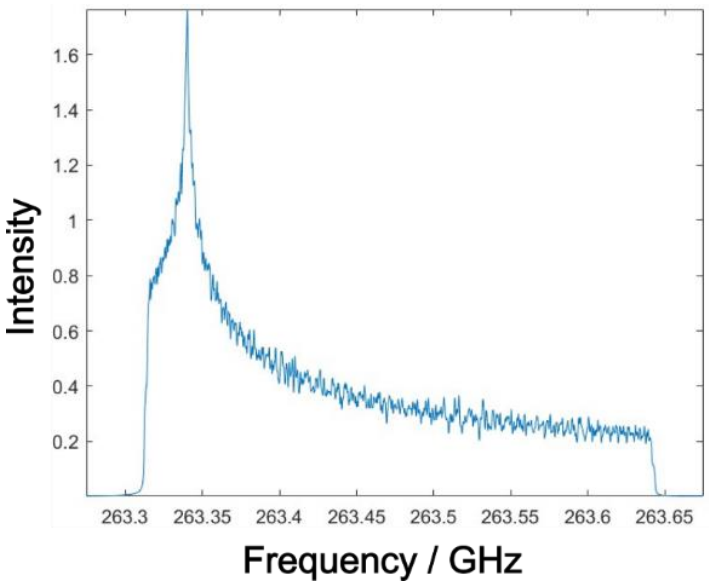

Figure 3.2.1 Simulated ESR spectrum of the electron spin with g = [2.0014, 2.0016, 2.0039].

With addition of one ^{1}H spin (I=1/2) and parameters set as follows:, MW power ω_1 = 1 MHz, MAS rate ω_r = 10 kHz, hyperfine interaction (dipolar interaction) between electron spin and ^{1}H spin A = [9 MHz, -4.5 MHz, -4.5 MHz] (distance between spins r ~ 0.26 nm)[81], relaxation time for electron spin T_{1e} = 100 μs, T_{2e} = 1 μs (typical relaxation times for electron spin[82]) and relaxation time for ^{1}H spin T_{1n} = 1 s, T_{2n} = 1 ms (relaxation times used as a series of value tested and no significant qualitative change). The powder grid used is 400 points three-angle REPULSION[83] grids.

The chirped MW (Figure 3.2.2) is in saw-tooth shape, centered at specific frequency and MW swept around the center frequency. The sweep widths tested in the simulations are 0, 50, 100, 200 and 350 MHz. Each sweep lasts 100 μs, which is also the rotor period for MAS. The total MW irradiation time is 10 s. The DNP with frequency sweep width 0 is equivalent to the conventional CW DNP.

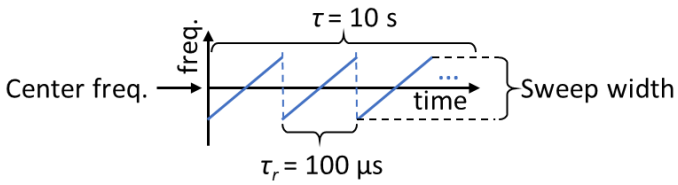

Figure 3.2.2 Schematic of the frequency sweep MW.

The simulated SE-DNP enhancement frequency profiles around positive enhancement peak is shown in Figure 3.2.3. The resulting spectra of sample under static state and sample under MAS are compared.

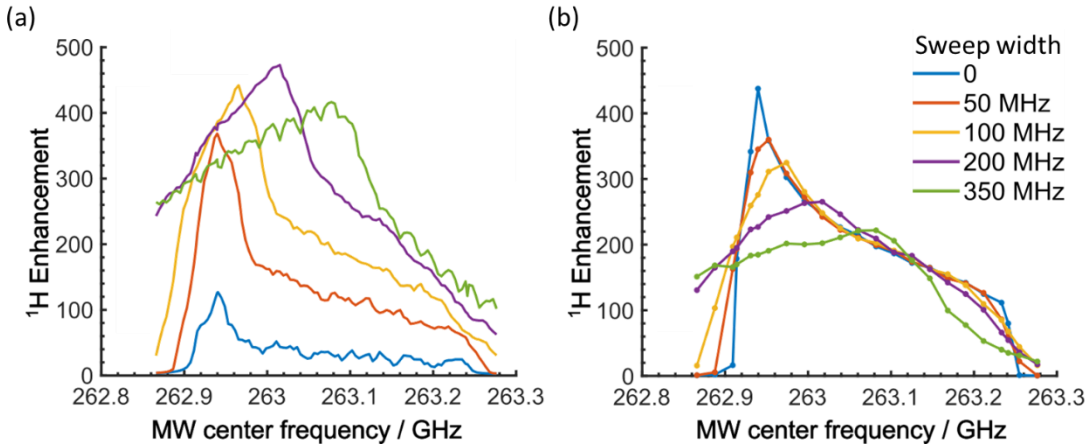

Figure 3.2.3 The simulated SE-DNP enhancement frequency profiles. MW with frequency sweep of 0, 50, 100, 200, 350 MHz on static sample (a) and sample under MAS (b) are compared.

It can be seen as expected, with chirped MW, the DNP enhancement is indeed greatly increased. The best DNP enhancement in this simulation is achieved with a ~200MHz frequency-sweep range. However, the chirped MW on the sample under MAS does not produce better DNP enhancement, but on the contrary, reduces it.

To elucidate the reason for this phenomenon, I analyzed the mechanism for SE-DNP

under MAS. For an 800 points three-angle REPULSION grids rotating under MAS, Figure 3.2.4(a) shows the SE positive matching condition for each of the points of orientation moving around during one rotor period (100 μs). Each curve corresponds to each of the points of orientation. And the color of the curves changes with the strength of hyperfine interaction along the time, which then represents the changes of estimated transition probability for each orientation at a certain time during the rotor period. A brighter color means higher transition probability. Thus, if the MW is applied at a certain frequency, while a curve crosses it at some point of time when with it has non-zero transition probability (non-zero hyperfine interaction). The MW will trigger SE for that certain point of orientation. Thus, with all these curves widely fluctuating in different patterns, it is generally difficult to design a straightforward modulated MW scheme to maximize the DNP enhancement.

Instead, the curves overlapping with each other create a bright horizontal line on the figure. This is the frequency where one would get the highest SE-DNP enhancement if CW MW is applied. Actually, the figure can be integrated along the time to get the integrated transition probability, which can predicate the CW DNP frequency profile after one rotor period, as shown in Figure 3.2.4(b). For a non-CW MW, the resulting DNP enhancement can also be predicted by integrating along the path of MW in Figure 3.2.4(a). It is clear that the MW to get the highest DNP enhancement is the CW MW with frequency of the horizontal line, going away from it makes the DNP enhancement worse. That is, in this case and for one rotor period, it is not beneficial using any multi-frequency MW.

While for steady state after MW irradiation for a long time, considering the effect of relaxation and equilibrium state, if the DNP enhancement from SE of the points of

orientation pass the best frequency are at least partially saturated, it may be beneficial to cover those points of orientation that is not passing the best frequency with frequency-sweep MW. However, for this already rather anisotropic *g* tensor, ~90% of SE matching condition already pass the best MW frequency. Covering the left 10% won't make up for the loss for straying away from the best frequency. As comparison, similar simulation shows ~85% of SE matching condition pass the best MW frequency for an axial *g* = [2.0013 2.0013 2.0043], and ~100% of SE matching condition pass the best MW frequency for a symmetry *g* = [2.0003 2.0023 2.0043].

For the SE-DNP of static sample, which has SE matching condition for each point of orientation being time-independent, it is easy to understand that chirped MW can cover all the matching conditions while the CW MW can only cover a few. To put it another way, in SE-DNP for sample under MAS, the MAS has already done the job that multi-frequency MW does for the static sample.

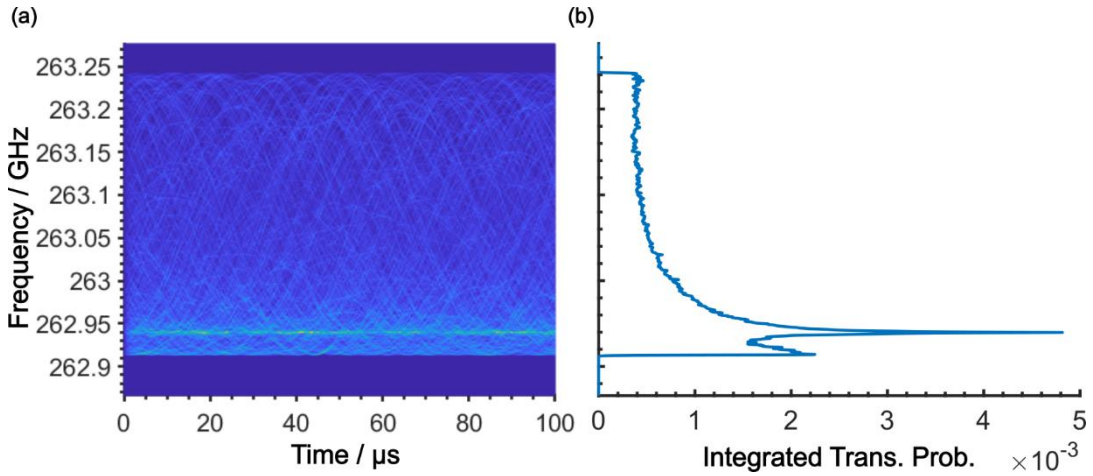

Figure 3.2.4 (a) SE positive matching condition for each of the point of orientation of the powder grids moving around during one rotor period, whose integration along the time is the predication of CW DNP frequency profile after one rotor period (b). (b) uses the same y axis ticks as (a).

3.3 Simulation Results: Solid-Effect DNP under MAS for Mixed Radicals

For SE under MAS with one single type of radical, it is difficult to benefit from using multi-frequency MW. Thus, I considered a more complex system, such as a hypothetical sample containing two types of radicals with different *g* tensor. Here, it is supposed that two types of radicals will not interfere with each other and only SE is considered. One radical has electron spin with g = [2.0014 2.0016 2.0039] (radical 1) and another has g = [2.0013 2.0023 2.0033] (radical 2). Each electron spin is paired with a ^{1}H spin with the same hyperfine interaction A = [9 MHz, -4.5 MHz, -4.5 MHz] but different randomized coordination. Other conditions are the same as the simulation of Figure 3.2.2.

Figure 3.3.1(a) shows the DNP enhancement frequency profile around positive enhancement peak after MW irritation for 10 s. The result of mixed radical 1 and 2 (blue solid curve) is compared with the results of only radical 1 (orange dashed curve) and only radical 2 (yellow dashed curve). Note that the enhancement is the ^{1}H intensity after DNP over the thermal equilibrium state ^{1}H intensity, and the mixed radical has 2 ^{1}H spins while the cases of using only radical 1 or 2 has 1 ^{1}H spin. Thus, the resulting frequency profile of mixed radical is like an average of the frequency profiles using only radical 1 or 2. Two peaks of maximum DNP enhancement can be observed in the mixed radical frequency profile. It can be expected if only applying CW MW on frequency 1 or frequency 2, which are also the best frequency when only use radical 1 or 2. It will be hard for MAS to cover the matching conditions for the other radical. Multi-frequency MW could be beneficial here.

To test this, I simulated DNP enhancement frequency profiles with 3 kinds of MW irradiation for 10 s. The first is CW MW on frequency 1 (262.93969 GHz), the second

is CW MW on frequency 2 (263.03169 GHz), the third is MW on frequency 1 for one rotor period (100 μs) then on frequency 2 for one rotor period and repeating this process. The results are shown in Figure 3.3.1(b). The simulated DNP enhancement for each point of the 400 point three-angle REPULSION grids is sorted and plotted as dots. And the dashed lines are the average enhancement of these points. Applying CW MW on frequency 1 (orange dots) leaves some points with very low DNP enhancement. This is the point of orientation of radical 2 that MAS could not bring to frequency 1. Appling CW MW on frequency 2 (yellow dots) do not have this problem but the overall DNP enhancement is relatively low compared to applying MW on both frequency 1 and 2 in turns (blue dots). Applying MW on frequency 1 and 2 in turns achieves a ~15% higher average DNP enhancement compared to applying CW MW. The idea is that for SE-DNP, multi-frequency MW could compensate MAS to achieve a higher DNP enhancement under specific conditions.

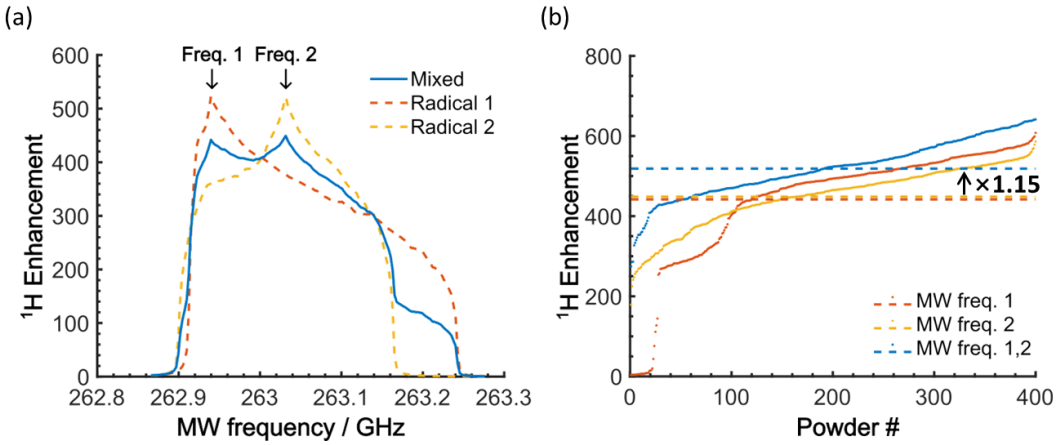

Figure 3.3.1 (a) DNP enhancement frequency profile for radical 1, radical 2 and mixed radicals 1, 2. The frequency 1 and frequency 2 are marked on the frequency profile, corresponding to the DNP enhancement peaks. (b) The DNP enhancement of each point (dots) of orientation of powder grid and the averaged values (dashed lines). Three colors correspond to CW MW on frequency 1 (orange), CW MW on frequency 2 (yellow) and MW on frequency 1 for one rotor period then on frequency 2 for one rotor period, repeating (blue).

3.4 Simulation Results: Solid-Effect DNP for Mn(II)

A realistic case that is similar to the mixed radicals is the DNP using Mn-DOTA.[84,85] The paramagnetic metal ion Mn(II) will not be reduced in the cytoplasm, thus, it is a potential PA for in-cell DNP-NMR. However, the DNP enhancement of such paramagnetic metal ion is often weaker than that of generally used radical PA. ESR spectrum of Mn(II) has a sextet splitting due to isotropic hyperfine interaction A_1 (Fermi contact interaction), which generates six positive SE-DNP enhancement peaks and six negative SE-DNP enhancement peaks. The hyperfine interaction A_1 of Mn(II) being isotropic, and much larger than its hyperfine interaction A_2 (dipolar interaction) with another nuclear spin, meaning MAS only modulates A_2 within each of the matching conditions, which are separated by the isotropic A_1. Thus, MAS cannot move the SE matching conditions to a single frequency, it should be beneficial to use multi-frequency MW to compensate for this. The spin dynamic simulation was conducted to explore this possibility. Due to the MAS being computationally heavy for this spin system, and the MAS modulated anisotropic interactions of the system should not affect the conclusion of this section, I conducted spin dynamic simulation with the spin system under static state.

First, as the preparation of DNP simulation, I simulated the ESR spectrum of Mn(II), including an electron spin (S=5/2, g=2.0023) and a Mn spin (I=5/2), as shown in Figure 3.4.1(a). The ESR spectrum indeed has six splitting peaks, showing the simulation works properly. Other parameters used are as follows: magnetic field B_0=9.4 T, hyperfine interaction between electron spin and Mn spin A_1 = 254 MHz, and zero field splitting D = 640 MHz, E = 100 MHz.[85] The powder grid used is 1600 points two-angle REPULSION grids.

Then, one nuclear spin ^{13}C (I=1/2) was added into the spin system. The SE-DNP frequency profile was simulated, showing six positive and six negative DNP enhancement peaks (Figure 3.4.1(b)). The two positive enhancement peaks are separated by hyperfine interaction constant, around 254 MHz. Other parameters were set as follows: temperature T = 20 K, hyperfine interaction between electron spin and ^{13}C spin A_2 = [9 MHz, -4.5 MHz, -4.5 MHz], relaxation time for electron spin T_{1e} = 100 μs, T_{2e} = 0.1 μs and relaxation time for ^{13}C spin T_{1n} = 0.1 s, T_{2n} = 1 ms. The powder grid used is 100 points two-angle REPULSION grids.

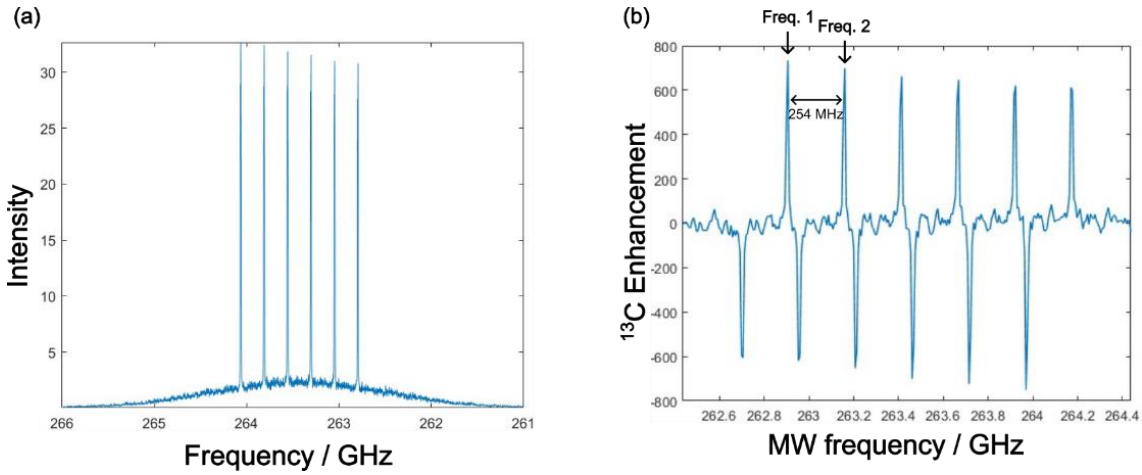

Figure 3.4.1 (a) Simulated the ESR spectrum of Mn(II) and (b) simulated ^{13}C DNP frequency profile using Mn(II) as PA. The frequencies of first two positive SE-DNP peaks are marked as frequency 1 and frequency 2.

The idea is to apply MW on both frequency 1 and frequency 2 (shown in Figure 3.4.1(b)) in turn. To test this, I simulated the following two cases. In case A, CW MW irradiation only on frequency 1 for 0.2 s. In case B, MW on frequency 1 for 0.5 μs and frequency 2 for 0.5 μs, repeating the process for 0.2 s (Figure 3.4.2(a)). The simulation was conducted for different MW power (MW Rabi frequency ω_1). The

results are shown in Figure 3.4.2(b). It can be seen, for the maximum DNP enhancement of case B, it is ~70% higher than that of case A. It is expected the mechanism of the improvement is with enough MW power, applying MW on frequency 1 for half of the time is enough to at least partially saturate the enhancement can be provided by the electron spin population there, thus, apply MW on two peaks in turns leads to a better total DNP enhancement. Byond the point of maximum DNP enhancement, the drop of enhancement can be understood that high MW power is broadband enough to excite the negative DNP enhancement condition, causing a lower total DNP enhancement.

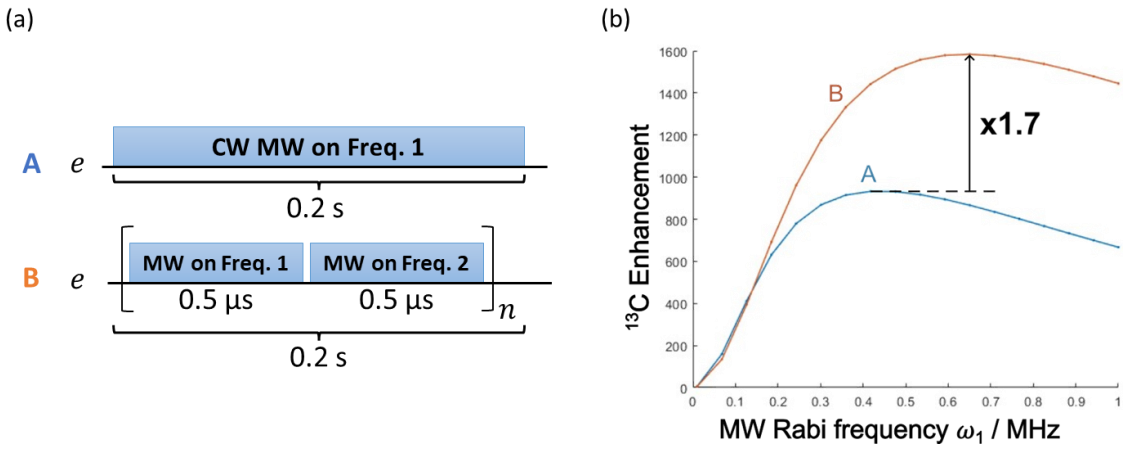

Figure 3.4.2 (a) The schematic of applying CW MW on frequency 1 (case A) and applying MW on frequency 1 and frequency 2 in turn (case B). (b) The simulated ^{13}C DNP enhancement with MW irradiation as case A or case B and with different MW power (MW Rabi frequency ω_1).

4. General Conclusion

To improve DNP spatial selectivity with multi-frequency MW, I proposed a new method for background signal suppression, which takes the difference between positively and negatively DNP-enhanced NMR spectra to selectively enhance the target signals in the presence of substantial background signals. I refer to this method as the opposite polarity subtraction (Oops) DNP. This approach requires some method to deliver the PA in the vicinity of the target molecules. Methods using bio-orthogonal chemical reactions[86] and signal peptides have been previously reported.[50] To validate the efficacy of the method, I used a reverse-micelle sample that enabled the PA (OX063 trityl) and the target (urea) to be confined within the reverse micelles and the external isooctane matrix to be used as the background. The efficacy of background suppression was evaluated using a contrast factor, defined as the ratio of the absolute value of the integral of the target and background peaks.

Three cases I compared in this study: (i) conventional positive DNP, (ii) the MW-off data subtraction, and (iii) the Oops procedure. A comparison of the results consisting of the time dependence of the contrast factors for these cases emphasizes that selecting an appropriate build-up time along with the Oops treatment is crucial for efficiently suppressing the background signal. In the demonstrative sample with an optimal build-up time of 60 s, the method achieved a contrast factor C = 12.9, which is much higher than C = 3.22 achieved with the conventional DNP and 0.56 with the MW-off data (i.e., regular MAS NMR). The maximum achievable contrast factor was also approximately twice higher than that of the MW-off data subtraction (C = 6.91) because it doubles the target signal intensity within the same total experiment time.

Simulations were conducted to gain deeper insights into the background signal

suppression method and its possible applications. Using a classical diffusion model, the parameters were optimized to globally fit the simulated build-up for experimental build-ups of target and background signals recorded under MW-off, DNP(+), and DNP(−) conditions. The resultant parameters aligned well with theoretical predictions and other experimental measurements. The simulation of the spatial polarization distribution highlighted the spatial selectivity of the method with a certain DNP build-up time. Alterations of the parameters demonstrated the performance of the background signal suppression method under various scenarios. For instance, variations in the sizes of the background did not substantially affect the method's efficiency. A faster nuclear spin relaxation rate can suppress the reach of the hyperpolarization in space, thereby facilitating the selection of an optimal build-up time to achieve the maximum contrast factor. Spin diffusion mediated by other types of nuclei, such as ^{1}H, is much faster than that mediated by the ^{13}C used in the sample. Faster spin diffusion would enable the targeted measurements to be applied to much larger molecular entities. To fully exploit the uniqueness of DNP-enhanced MAS NMR as a valid method for analyzing a complex mixture sample with high sensitivity, proper treatment of background signals from the not-of-interest region is a critical problem. The simple methods described here would provide a valid option for expanding the applicability of DNP MAS NMR for intracellular structural biology and other unexplored applications by reducing annoyance from backgrounds.

In the pursuit of improving DNP efficiency, this study investigated the application of multi-frequency-excitation DNP through spin dynamic simulations. The findings showed that, consistent with prior research, chirped microwave (MW) irradiation substantially boosts SE-DNP efficiency in static samples. However, this enhancement does not extend to samples under MAS, where, contrarily, DNP efficiency is

diminished.

Further examination of the SE-DNP matching conditions for a MAS cycle revealed the differences between static and MAS conditions. MAS induces a periodic motion in the SE-DNP matching conditions, leading to an overlap that creates advantageous fixed-frequency matching conditions for CW MW irradiation. However, the simulations under MAS with mixed radicals suggest that multi-frequency MW irradiation could be beneficial in more complex systems. A specific case is the simulations focusing on a practical scenario involving Mn(II)-based DNP, which shows greatly improved DNP efficiency using multi-frequency excitation MW.

The study overall demonstrates the potential of multi-frequency excitation DNP in achieving not only higher DNP efficiency but also enhanced spatial selectivity. The significant potential of frequency-agile MW sources is evident, especially considering polarizing agents like Mn(II) and nanodiamonds, which hold promise for in-cell DNP-NMR applications. Thus, multi-frequency excitation DNP could pave the way for high-sensitivity, spatially selective in-cell DNP-NMR.

The practical application of the Oops DNP and other ideas proposed in this dissertation is restricted to our currently equipped MW sources and a few advanced instruments in other laboratories. Due to the uniqueness of our tunable gyrotron and the limited MW power of the solid-state source, methods in this dissertation may not be instantly available to many other DNP-NMR users. With the development of frequency-agile MW sources in future, it is expected the limited maximum power and maximum operational magnetic field will be gradually improved and they will be generally adopted by more and more DNP-NMR researchers. By then, the study of this dissertation should have more practical applications and more sophisticated multi-

frequency-excitation DNP schemes can be devised, simulated, and put into experimental validation.

5. Acknowledgement

This research was carried out under the supervision of Professor Dr. Toshimichi Fujiwara and Associate Professor Dr. Yoh Matsuki. I deeply appreciate the opportunity of conducting this research and the invaluable instruction.

I deeply appreciate the advice and discussion from Dr. Hajime Tamaki, Dr. Ken Kato and Dr. Tomoaki Sugishita.

I appreciate Dr. Ayako Egawa for supporting the research.

I thank Mr. Xin Zhang for learning from each other.

I thank Institute for Protein Research for the financial support during my study.

6. Reference

1. Keeler, J. *Understanding NMR Spectroscopy*. (John Wiley & Sons, 2010).
2. Levitt, M. H. *Spin Dynamics: Basics of Nuclear Magnetic Resonance*. (John Wiley & Sons, 2013).
3. Cavanagh, J. *Protein NMR Spectroscopy: Principles and Practice*. (Academic press, 1996).
4. Schmidt-Rohr, K. & Spiess, W. S. *Multidimensional Solid-State NMR and Polymers*. (Academic Press, 1994).
5. Reif, B., Ashbrook, S. E., Emsley, L. & Hong, M. Solid-state NMR spectroscopy. *Nature Reviews Methods Primers* **1**, 2 (2021).
6. Polenova, T., Gupta, R. & Goldbourt, A. Magic Angle Spinning NMR Spectroscopy: A Versatile Technique for Structural and Dynamic Analysis of Solid-Phase Systems. *Analytical Chemistry* **87**, 5458–5469 (2015).
7. Kolodziejski, W. & Klinowski, J. Kinetics of Cross-Polarization in Solid-State NMR: A Guide for Chemists. *Chemical Reviews* **102**, 613–628 (2002).
8. Khago, D., Fucci, I. J. & Byrd, R. A. The Role of Conformational Dynamics in the Recognition and Regulation of Ubiquitination. *Molecules* **25**, 5933 (2020).
9. Markwick, P. R. L., Malliavin, T. & Nilges, M. Structural Biology by NMR: Structure, Dynamics, and Interactions. *PLOS Computational Biology* **4**, e1000168 (2008).
10. Wang, H. & Wang, J. How cryo-electron microscopy and X-ray crystallography complement each other. *Protein Science* **26**, 32–39 (2017).
11. Novoa-Carballal, R., Fernandez-Megia, E., Jimenez, C. & Riguera, R. NMR methods for unravelling the spectra of complex mixtures. *Natural Product Reports*. **28**, 78–98 (2011).
12. Forseth, R. R. & Schroeder, F. C. NMR-spectroscopic analysis of mixtures: from structure to function. *Current Opinion in Chemical Biology* **15**, 38–47 (2011).
13. Chordia, S., Narasimhan, S., Lucini Paioni, A., Baldus, M. & Roelfes, G. In Vivo Assembly of Artificial Metalloenzymes and Application in Whole-Cell Biocatalysis**. *Angewandte Chemie International Edition* **60**, 5913–5920 (2021).
14. Speer, S. L. *et al.* The intracellular environment affects protein–protein interactions. *Proceedings of the National Academy of Sciences* **118**, e2019918118 (2021).
15. Sakakibara, D. *et al.* Protein structure determination in living cells by in-cell NMR spectroscopy. *Nature* **458**, 102–105 (2009).
16. Inomata, K. *et al.* High-resolution multi-dimensional NMR spectroscopy of proteins in human cells. *Nature* **458**, 106–109 (2009).
17. DeMott, C. M., Majumder, S., Burz, D. S., Reverdatto, S. & Shekhtman, A. Ribosome Mediated Quinary Interactions Modulate In-Cell Protein Activities. *Biochemistry* **56**, 4117–4126 (2017).
18. Lu, J.-X. *et al.* Molecular Structure of β-Amyloid Fibrils in Alzheimer's Disease Brain

Tissue. *Cell* **154**, 1257–1268 (2013).

19. Dettmer, U., Selkoe, D. & Bartels, T. New insights into cellular α-synuclein homeostasis in health and disease. *Current Opinion in Neurobiology* **36**, 15–22 (2016).

20. Moriya, H. Quantitative nature of overexpression experiments. *Molecular Biology of the Cell* **26**, 3932–3939 (2015).

21. Chan, Y.-H. M. & Marshall, W. F. Organelle Size Scaling of the Budding Yeast Vacuole Is Tuned by Membrane Trafficking Rates. *Biophysical Journal* **106**, 1986–1996 (2014).

22. Łabędź, B., Wańczyk, A. & Rajfur, Z. Precise mass determination of single cell with cantilever-based microbiosensor system. *PLoS One* **12**, e0188388 (2017).

23. Maldonado, A. Y., Burz, D. S. & Shekhtman, A. In-cell NMR spectroscopy. *Progress in Nuclear Magnetic Resonance Spectroscopy* **59**, 197–212 (2011).

24. Verardi, R., Traaseth, N. J., Masterson, L. R., Vostrikov, V. V. & Veglia, G. Isotope Labeling for Solution and Solid-State NMR Spectroscopy of Membrane Proteins. in 35–62 (2012). Isotope labeling in Biomolecular NMR. Advances in Experimental Medicine and Biology, vol 992. Springer, Dordrecht.

25. Rowlinson, B., Crublet, E., Kerfah, R. & Plevin, M. J. Specific isotopic labelling and reverse labelling for protein NMR spectroscopy: using metabolic precursors in sample preparation. *Biochemical Society Transactions* **50**, 1555–1567 (2022).

26. Zhang, Y. *et al.* Membrane Protein Structures in Native Cellular Membranes Revealed by Solid-State NMR Spectroscopy. *JACS Au* **3**, 3412–3423 (2023).

27. Luchinat, E. & Banci, L. In-Cell NMR in Human Cells: Direct Protein Expression Allows Structural Studies of Protein Folding and Maturation. *Accounts of Chemical Research* **51**, 1550–1557 (2018).

28. Lilly Thankamony, A. S., Wittmann, J. J., Kaushik, M. & Corzilius, B. Dynamic nuclear polarization for sensitivity enhancement in modern solid-state NMR. *Progress in Nuclear Magnetic Resonance Spectroscopy* **102–103**, 120–195 (2017).

29. Pinon, A. C. *et al.* Measuring Nano- to Microstructures from Relayed Dynamic Nuclear Polarization NMR. *The Journal of Physical Chemistry C* **121**, 15993–16005 (2017).

30. Eills, J. *et al.* Spin Hyperpolarization in Modern Magnetic Resonance. *Chemical Reviews* **123**, 1417–1551 (2023).

31. Menzildjian, G. *et al.* Polarizing agents for efficient high field DNP solid-state NMR spectroscopy under magic-angle spinning: from design principles to formulation strategies. *Chemical Science* **14**, 6120–6148 (2023).

32. Corzilius, B. Paramagnetic metal ions for dynamic nuclear polarization. *eMagRes* **7**, (2018).

33. Chakrabarty, T., Goldin, N., Feintuch, A., Houben, L. & Leskes, M. Paramagnetic Metal-Ion Dopants as Polarization Agents for Dynamic Nuclear Polarization NMR Spectroscopy in Inorganic Solids. *ChemPhysChem* **19**, 2139–2142 (2018).

34. Rej, E., Gaebel, T., Boele, T., Waddington, D. E. J. & Reilly, D. J. Hyperpolarized

nanodiamond with long spin-relaxation times. *Nature Communications* **6**, 8459 (2015).

35. Yoon, D. *et al.* High-Field ^{13} C Dynamic Nuclear Polarization in Nanodiamond. *The Journal of Physical Chemistry C* **123**, 21237–21243 (2019).

36. Hovav, Y., Feintuch, A. & Vega, S. Theoretical aspects of dynamic nuclear polarization in the solid state – The solid effect. *Journal of Magnetic Resonance* **207**, 176–189 (2010).

37. Equbal, A., Leavesley, A., Jain, S. K. & Han, S. Cross-Effect Dynamic Nuclear Polarization Explained: Polarization, Depolarization, and Oversaturation. *The Journal of Physical Chemistry Letters* **10**, 548–558 (2019).

38. Thurber, K. R. & Tycko, R. Theory for cross effect dynamic nuclear polarization under magic-angle spinning in solid state nuclear magnetic resonance: The importance of level crossings. *The Journal of Chemical Physics* **137**, (2012).

39. Wenckebach, W. Th. Dynamic nuclear polarization via thermal mixing: Beyond the high temperature approximation. *Journal of Magnetic Resonance* **277**, 68–78 (2017).

40. Cheung, T. T. P. Spin diffusion in NMR in solids. *Physical Review B* **23**, 1404–1418 (1981).

41. Tatman, B. P., Franks, W. T., Brown, S. P. & Lewandowski, J. R. Nuclear spin diffusion under fast magic-angle spinning in solid-state NMR. *The Journal of Chemical Physics* **158**, (2023).

42. Ackermann, B. E., Lim, B. J., Elathram, N., Narayanan, S. & Debelouchina, G. T. A Comparative Study of Nitroxide-Based Biradicals for Dynamic Nuclear Polarization in Cellular Environments. *ChemBioChem* **23**, (2022).

43. Hovav, Y., Feintuch, A., Vega, S. & Goldfarb, D. Dynamic nuclear polarization using frequency modulation at 3.34 T. *Journal of Magnetic Resonance* **238**, 94–105 (2014).

44. Can, T. V., Weber, R. T., Walish, J. J., Swager, T. M. & Griffin, R. G. Frequency-Swept Integrated Solid Effect. *Angewandte Chemie International Edition* **56**, 6744–6748 (2017).

45. Ajoy, A. *et al.* Enhanced dynamic nuclear polarization via swept microwave frequency combs. *Proceedings of the National Academy of Sciences* **115**, 10576–10581 (2018).

46. Equbal, A., Tagami, K. & Han, S. Pulse-Shaped Dynamic Nuclear Polarization under Magic-Angle Spinning. *The Journal of Physical Chemistry Letters* **10**, 7781–7788 (2019).

47. Viennet, T. *et al.* Selective Protein Hyperpolarization in Cell Lysates Using Targeted Dynamic Nuclear Polarization. *Angewandte Chemie International Edition* **55**, 10746–10750 (2016).

48. Marin-Montesinos, I. *et al.* Selective high-resolution DNP-enhanced NMR of biomolecular binding sites. *Chemical Science* **10**, 3366–3374 (2019).

49. Gauto, D., Dakhlaoui, O., Marin-Montesinos, I., Hediger, S. & De Paëpe, G. Targeted DNP for biomolecular solid-state NMR. *Chemical Science* **12**, 6223–6237 (2021).

50. Albert, B. J. *et al.* Dynamic Nuclear Polarization Nuclear Magnetic Resonance in Human Cells Using Fluorescent Polarizing Agents. *Biochemistry* **57**, 4741–4746

(2018).

51. Matsuki, Y., Idehara, T., Fukazawa, J. & Fujiwara, T. Advanced instrumentation for DNP-enhanced MAS NMR for higher magnetic fields and lower temperatures. *Journal of Magnetic Resonance* **264**, 107–115 (2016).

52. Guy, M. L., Zhu, L. & Ramanathan, C. Design and characterization of a W-band system for modulated DNP experiments. *Journal of Magnetic Resonance* **261**, 11–18 (2015).

53. Sato, K. *et al.* Trityl-Aryl-Nitroxide-Based Genuinely *g* -Engineered Biradicals, As Studied by Dynamic Nuclear Polarization, Multifrequency ESR/ENDOR, Arbitrary Wave Generator Pulse Microwave Waveform Spectroscopy, and Quantum Chemical Calculations. *The Journal of Physical Chemistry A* **123**, 7507–7517 (2019).

54. Scott, F. J. *et al.* Frequency-agile gyrotron for electron decoupling and pulsed dynamic nuclear polarization. *Journal of Magnetic Resonance* **289**, 45–54 (2018).

55. B. Tamamushi & N. Watanabe. The formation of molecular aggregation structures in ternary system: Aerosol OT/water/iso-octane. *Colloid and Polymer Science* **258**, 174–178 (1980).

56. Suzuki, A. & Yui, H. Spectroscopic study of the melting and reconstruction of sodium bis(2-ethylhexyl) sulfosuccinate (AOT) reverse micelles from their frozen states. *Journal of Colloid and Interface Science* **443**, 188–196 (2015).

57. Leavesley, A., Wilson, C. B., Sherwin, M. & Han, S. Effect of water/glycerol polymorphism on dynamic nuclear polarization. *Physical Chemistry Chemical Physics* **20**, 9897–9903 (2018).

58. Tamamushi, B. & Watanabe, N. The formation of molecular aggregation structures in ternary system: Aerosol OT/water/iso-octane. *Colloid and Polymer Science* **258**, 174–178 (1980).

59. Feitosa, E., Cavalcante, V. R. O. & Amaral, L. Q. Phase behavior of the orange essential oil/sodium bis(2-ethylhexyl)sulfosuccinate/water system. *Colloids and Surfaces A: Physicochemical and Engineering Aspects* **348**, 82–86 (2009).

60. Alger, D. B. The water solubility of 2-butanol: A widespread error. *Journal of Chemical Education* **68**, 939 (1991).

61. Gambill, W. R. How to estimate mixtures viscosities. *Chemical Engineering* **66**, 151–152 (1959).

62. Kotlarchyk, M., Huang, J. S. & Chen, S. H. Structure of AOT reversed micelles determined by small-angle neutron scattering. *The Journal of Physical Chemistry* **89**, 4382–4386 (1985).

63. Matsuki, Y., Nakamura, S., Fukui, S., Suematsu, H. & Fujiwara, T. Closed-cycle cold helium magic-angle spinning for sensitivity-enhanced multi-dimensional solid-state NMR. *Journal of Magnetic Resonance* **259**, 76–81 (2015).

64. Matsuki, Y. & Fujiwara, T. Cryogenic Platforms and Optimized DNP Sensitivity. in *eMagRes* vol. 7 9–24 (2018).

65. Fung, B. M., Khitrin, A. K. & Ermolaev, K. An Improved Broadband Decoupling Sequence for Liquid Crystals and Solids. *Journal of Magnetic Resonance* **142**, 97–101

(2000).

66. Wang, X. *et al.* Direct dynamic nuclear polarization of 15N and 13C spins at 14.1 T using a trityl radical and magic angle spinning. *Solid State Nuclear Magnetic Resonance* **100**, 85–91 (2019).

67. Lindeman, L. P. & Adama, J. Q. Carbon-13 nuclear magnetic resonance spectrometry. Chemical shifts for the paraffins through C9. *Analytical Chemistry* **43**, 1245–1252 (1971).

68. Ejchart, A. Substituent effects on ^{13} C NMR. 2—chemical shifts in the saturated framework of secondary aliphatic derivatives. *Organic Magnetic Resonance* **15**, 22–24 (1981).

69. Clauss, J., Schmidt-Rohr, K. & Spiess, H. W. Determination of domain sizes in heterogeneous polymers by solid-state NMR. *Acta Polymerica* **44**, 1–17 (1993).

70. Chen, Q. & Schmidt-Rohr, K. Measurement of the local 1H spin-diffusion coefficient in polymers. *Solid State Nuclear Magnetic Resonance* **29**, 142–152 (2006).

71. Kaushik, M. *et al.* Gd(iii) and Mn(ii) complexes for dynamic nuclear polarization: small molecular chelate polarizing agents and applications with site-directed spin labeling of proteins. *Physical Chemistry Chemical Physics* **18**, 27205–27218 (2016).

72. Khutsishvili, G. R. Spin diffusion. *Uspekhi Fizicheskih Nauk* **87**, 211–254 (1965).

73. Björgvinsdóttir, S., Walder, B. J., Pinon, A. C. & Emsley, L. Bulk Nuclear Hyperpolarization of Inorganic Solids by Relay from the Surface. *Journal of the American Chemical Societ* **140**, 7946–7951 (2018).

74. Björgvinsdóttir, S., Moutzouri, P., Berruyer, P., Hope, M. A. & Emsley, L. Sensitivity Enhancements in Lithium Titanates by Incipient Wetness Impregnation DNP NMR. *The Journal of Physical Chemistry C* **124**, 16524–16528 (2020).

75. Matsuki, Y., Sugishita, T. & Fujiwara, T. Surface-Only Spectroscopy for Diffusion-Limited Systems Using Ultra-Low-Temperature DNP MAS NMR at 16.4 T. *The Journal of Physical Chemistry C* **124**, 18609–18614 (2020).

76. Matsuki, Y., Idehara, T., Fukazawa, J. & Fujiwara, T. Advanced instrumentation for DNP-enhanced MAS NMR for higher magnetic fields and lower temperatures. *Journal of Magnetic Resonance* **264**, 107–115 (2016).

77. Hogben, H. J., Krzystyniak, M., Charnock, G. T. P., Hore, P. J. & Kuprov, I. Spinach – A software library for simulation of spin dynamics in large spin systems. *Journal of Magnetic Resonance* **208**, 179–194 (2011).

78. Kuprov, I. Diagonalization-free implementation of spin relaxation theory for large spin systems. *Journal of Magnetic Resonance* **209**, 31–38 (2011).

79. Krzystyniak, M., Edwards, L. J. & Kuprov, I. Destination state screening of active spaces in spin dynamics simulations. *Journal of Magnetic Resonance* **210**, 228–232 (2011).

80. Edwards, L. J. & Kuprov, I. Parallel density matrix propagation in spin dynamics simulations. *The Journal of Chemical Physics* **136**, (2012).

81. Schweiger, A. & Jeschke, G. *Principles of Pulse Electron Paramagnetic Resonance*.

(Oxford University Press, 2001).

82. Sato, H. *et al.* Electron spin–lattice relaxation of nitroxyl radicals in temperature ranges that span glassy solutions to low-viscosity liquids. *Journal of Magnetic Resonance* **191**, 66–77 (2008).

83. Bak, M. & Nielsen, N. C. REPULSION, A Novel Approach to Efficient Powder Averaging in Solid-State NMR. *Journal of Magnetic Resonance* **125**, 132–139 (1997).

84. Keller, K. *et al.* EPR characterization of Mn(ii) complexes for distance determination with pulsed dipolar spectroscopy. *Physical Chemistry Chemical Physics* **18**, 25120–25135 (2016).

85. Kaushik, M. *et al.* Gd(iii) and Mn(ii) complexes for dynamic nuclear polarization: small molecular chelate polarizing agents and applications with site-directed spin labeling of proteins. *Physical Chemistry Chemical Physics* **18**, 27205–27218 (2016).

86. Lim, B. J., Ackermann, B. E. & Debelouchina, G. T. Targetable Tetrazine-Based Dynamic Nuclear Polarization Agents for Biological Systems. *ChemBioChem* **21**, 1315–1319 (2020).